REPUBLIC OF TÜRKİYE

YILDIZ TECHNICAL UNIVERSITY

GRADUATE SCHOOL OF NATURAL AND APPLIED SCIENCES

SAMARIUM AND THULIUM DOPED LUMINESCENT GLASS-BASED LEDS IN INDOOR AGRICULTURE APPLICATIONS AND THEIR EFFECTS ON PLANT GROWTH

Utku EKİM

MASTER OF SCIENCE THESIS

Department of Metallurgical and Materials Engineering

Materials Program

Supervisor

Assoc. Prof. Dr. Ali Erçin ERSUNDU

August, 2023

REPUBLIC OF TÜRKİYE

YILDIZ TECHNICAL UNIVERSITY

GRADUATE SCHOOL OF NATURAL AND APPLIED SCIENCES

SAMARIUM AND THULIUM DOPED LUMINESCENT GLASS-BASED LEDS IN INDOOR AGRICULTURE APPLICATIONS AND THEIR EFFECTS ON PLANT GROWTH

A thesis submitted by Utku EKİM in partial fulfillment of the requirements for the degree of MASTER OF SCIENCE is approved by the committee on 04.08.2023 in Department of Metallurgical and Materials Engineering.

Assoc. Prof. Dr. Ali Erçin ERSUNDU
Yıldız Technical University
Supervisor

Approved By the Examining Committee

Assoc. Prof. Dr. Ali Erçin ERSUNDU, Supervisor
Yıldız Technical University _____

Assoc. Prof. Dr. Fatih AKYOL
Yıldız Technical University _____

Prof. Dr. Esra ÖZKAN ZAYİM

Istanbul Technical University _____

I hereby declare that I have obtained the required legal permissions during data collection and exploitation procedures, that I have made the in-text citations and cited the references properly, that I haven't falsified and/or fabricated research data and results of the study and that I have abided by the principles of the scientific research and ethics during my Thesis Study under the title of Samarium and Thulium Doped Luminescent Glass-Based LEDs in Indoor Agriculture Applications and Their Effects on Plant Growth supervised by my supervisor, Assoc. Prof. Dr. Ali Erçin ERSUNDU. In the case of a discovery of false statement, I am to acknowledge any legal consequence.

Utku EKİM

Signature

This work was supported by Yildiz Technical University Scientific Research Projects Coordination Unit under project number FYL-2022-5156.

Dedicated to my ever-supportive parents

ACKNOWLEDGEMENTS

I wish to begin this report by expressing my gratitude to my supervisor, Assoc. Prof. Dr. Ali Erçin ERSUNDU, who has supported me throughout this process. I would not have advanced in my studies without his active inspiration, support, and guiding. I should also note that my supervisor, Prof. Dr. Miray ÇELİKBİLEK ERSUNDU, deserves a special mention for her diligent guidance and support throughout my years as a student. Being their student has always been a pleasant privilege for me.

At YTU Glass Research Group, I have been incredibly blessed to have a number of fantastic friends with brilliant minds who have also been a source of support over the years. The degree to which social and professional circles overlap has truly enhanced the pleasure of working. All of my friends who have worked with and guided me over the years have become a part of my family. I am grateful to all of them for their contribution to me.

I would like to thank my mother and father, who have helped me get to where I am in my life, who have supported me, guided me and never spared their love throughout my entire education and sports career and even in my current business life.

Finally, I want to thank my one and only partner—with whom I have been in a relationship since high school—for giving me the sense that I am never alone in life by supporting me in all of my endeavors, including competitions, exams, and life's challenges.

Utku EKİM

TABLE OF CONTENTS

ACKNOWLEDGEMENTS **v**
TABLE OF CONTENTS **vi**
LIST OF SYMBOLS **vii**
LIST OF ABBREVIATIONS **viii**
LIST OF FIGURES **ix**
LIST OF TABLES **xii**
ABSTRACT **xiii**
ÖZET **xv**
1 INTRODUCTION **1**
1.1 Literature Review 1
1.2 Objective of Thesis 3
1.3 Hypothesis 3
2 THEORETICAL INFORMATION **4**
2.1 Effect of Light on Plant Growth 4
2.2 Light Management in Greenhouses 6
2.3 Luminescence 9
2.4 Photoluminescent Materials Used in LEDs 12
3 EXPERIMENTAL STUDIES **14**
3.1 Sample Synthesis 14
3.2 Sample Characterization 15
3.3 Plant Tests 18
4 RESULTS **20**
4.1 Results 20
4.2 Discussion 45
4.3 Conclusion and Future Outlook 62
REFERENCES **65**
PUBLICATIONS FROM THE THESIS **76**

LIST OF SYMBOLS

SR_{ch-a}	Chlorophyll a
SR_{ch-b}	Chlorophyll b
°C	Degree Celsius
T_g	Glass Transition Temperature
nm	Nanometer
S/R	Ratio of shoot and root
rpm	Revolutions per minute
λ	Wavelength

LIST OF ABBREVIATIONS

CCT	Correlated Color Temperature
Chl-a	Chloropyll a
Chl-b	Chloropyll b
CIE	Commission Internationale de l'Éclariage (International Commission on Illumination)
CRI	Color Rendering Index
DLI	Daily Light Integral
DS	Downshifting
DW	Dry Weight
FW	Fresh Weight
LED	Light Emitting Diode
LUMO	Lowest Occupied Molecular Orbit
PAR	Photosynthetically Active Radiation
PiG	Phosphor in Glass
PL	Photoluminescence
PLE	Photoluminescence Excitation
PLQY	Photoluminescence Quantum Yield
PPFD	Photosynthetic Photon Flux Density
STA	Simultaneous Thermal Analysis
TCPC	Time-correlated Single-photon Counting
QC	Down-Conversion
UC	Up-conversion
UV	Ultraviolet
VIS	Visible
XRD	X-Ray Diffraction

LIST OF FIGURES

Figure 2.1 The three energy transfer processes……...…..……11

Figure 3.1 a) Glass batch homogenization in agate mortar, b) glass batches in platinum crucibles, c) steel mold that glass poured…….……14

Figure 4.1 Macro picture of $0.125Sm_2O_3 – 0.125Tm_2O_3$ sample…….……20

Figure 4.2 XRD pattern of $0.125Sm_2O_3 – 0.125Tm_2O_3$ sample……...21

Figure 4.3 STA analysis of $0.125Sm_2O_3 – 0.125Tm_2O_3$ sample…….….21

Figure 4.4 Optical absorption spectrum of $0.125Sm_2O_3 – 0.125Tm_2O_3$ sample……..22

Figure 4.5 PL excitation spectrums for different emission wavelengths of $0.125Sm_2O_3 – 0.125Tm_2O_3$ sample…….…….23

Figure 4.6 PL emission spectra of $0.125Sm_2O_3 – 0.125Tm_2O_3$ sample under 360 nm excitation…….…….24

Figure 4.7 Macro photo of $0.125Sm_2O_3 – 0.125Tm_2O_3$ sample under 360 nm excitation…….…….24

Figure 4.8 CIE color coordinates of $0.125Sm_2O_3 – 0.125Tm_2O_3$ sample under 360 nm excitation…….…….25

Figure 4.9 Macro picture of $0.125Sm_2O_3 – 0.25Tm_2O_3$ sample…….25

Figure 4.10 XRD pattern of $0.125Sm_2O_3 – 0.25Tm_2O_3$ sample…….26

Figure 4.11 STA analysis of $0.125Sm_2O_3 – 0.25Tm_2O_3$ sample……26

Figure 4.12 Optical absorption spectrum of $0.125Sm_2O_3 – 0.25Tm_2O_3$ sample……..…27

Figure 4.13 PL excitation spectrums for different emission wavelengths of $0.125Sm_2O_3$-$0.25Tm_2O_3$ sample……...…..…28

Figure 4.14 PL emission spectra of $0.125Sm_2O_3 – 0.25Tm_2O_3$ sample under 360 nm excitation……...…29

Figure 4.15 Macro photo of $0.125Sm_2O_3 – 0.25Tm_2O_3$ sample under 360 nm excitation……...….29

Figure 4.16 CIE color coordinates of $0.125Sm_2O_3 – 0.25Tm_2O_3$ sample under 360 nm excitation…….……..…….30

Figure 4.17 Macro picture of $0.25Sm_2O_3 – 0.125Tm_2O_3$ sample……...…30

Figure 4.18 XRD pattern of $0.25Sm_2O_3 – 0.125Tm_2O_3$ sample…….31

Figure 4.19 STA analysis of $0.25Sm_2O_3 – 0.125Tm_2O_3$ sample……31

Figure 4.20 Optical absorption spectrum of $0.25Sm_2O_3 – 0.125Tm_2O_3$ sample……32

Figure 4.21 PL excitation spectrums for different emission wavelengths of $0.25Sm_2O_3 – 0.125Tm_2O_3$ sample……...……..33

Figure 4.22 PL emission spectra of $0.25Sm_2O_3 – 0.125Tm_2O_3$ sample under 360 nm excitation……..…….……34

Figure 4.23 Macro photo of $0.25Sm_2O_3 – 0.125Tm_2O_3$ sample under 360 nm excitation……..……...……34

Figure 4.24 CIE color coordinates of $0.25Sm_2O_3 – 0.125Tm_2O_3$ sample under 360 nm excitation…….…….35

Figure 4.25 Macro picture of $0.25Sm_2O_3 – 0.25Tm_2O_3$ sample……..….35

Figure 4.26 XRD pattern of $0.25Sm_2O_3 – 0.25Tm_2O_3$ sample……36

Figure 4.27 STA analysis of $0.25Sm_2O_3 – 0.25Tm_2O_3$ sample……36

Figure 4.28 Optical absorption spectrum of $0.25Sm_2O_3 – 0.25Tm_2O_3$ sample……..…..37

Figure 4.29 PL excitation spectrums for different emission wavelengths of $0.25Sm_2O_3 – 0.25Tm_2O_3$ sample……38

Figure 4.30 PL emission spectra of $0.25Sm_2O_3 – 0.25Tm_2O_3$ sample under 360 nm excitation……..……39

Figure 4.31 Macro photo of $0.25Sm_2O_3 – 0.25Tm_2O_3$ sample under 360 nm excitation…….…….39

Figure 4.32 CIE color coordinates of $0.25Sm_2O_3 – 0.25Tm_2O_3$ sample under 360 nm excitation…….…..…40

Figure 4.33 Macro picture of $0.50Sm_2O_3 – 0.50Tm_2O_3$ sample……...40

Figure 4.34 XRD pattern of $0.50Sm_2O_3 – 0.50Tm_2O_3$ sample…….....…41

Figure 4.35 STA analysis of $0.50Sm_2O_3 – 0.50Tm_2O_3$ sample……..…..…41

Figure 4.36 Optical absorption spectrum of $0.50Sm_2O_3 – 0.50Tm_2O_3$ sample……...….42

Figure 4.37 PL excitation spectrums for different emission wavelengths of $0.50Sm_2O_3 – 0.50Tm_2O_3$ sample…….....…..…43

Figure 4.38 PL emission spectra of $0.50Sm_2O_3 – 0.50Tm_2O_3$ sample under 360 nm excitation…….……44

Figure 4.39 Macro photo of $0.50Sm_2O_3 – 0.50Tm_2O_3$ sample under 360 nm excitation…….……44

Figure 4.40 CIE color coordinates of $0.50Sm_2O_3 – 0.50Tm_2O_3$ sample under 360 nm excitation…….……45

Figure 4.41 a) XRD pattern, and b) STA thermogram, showing amorphous nature and thermal behavior of produced glass samples, respectively……...…46

Figure 4.42 Optical absorption spectrum of Sm^{3+} and Tm^{3+} co-doped glass samples…….……47

Figure 4.43 Excitation spectra of Sm^{3+} and Tm^{3+} co-doped glasses, with a) monitoring of 454 nm Tm^{3+} ion emission, b) monitoring of 648 nm Sm^{3+} ion emission……..…..48

Figure 4.44 Intersection area for PL excitation of Sm^{3+} and Tm^{3+} ions for selected $0.25Sm_2O_3$ - $0.25Tm_2O_3$ sample……..…….48

Figure 4.45 PL emission spectrums of the Sm^{3+} and Tm^{3+} co-doped glasses under 360 nm excitation……...…49

Figure 4.46 CIE color coordinates of Sm^{3+} and Tm^{3+} co-doped glasses under 360 nm excitation……..……50

Figure 4.47 a) PL emission spectrum and b) Lifetime analysis for Sample 1……...…51

Figure 4.48 a) PL emission spectrum and b) Lifetime analysis for Sample 2……...…52

Figure 4.49 Time-resolved PL spectra of (a) $0.25Tm_2O_3$ (Sample 1) and $0.25Sm_2O_3$ – $0.25Tm_2O_3$ samples for 454 nm emission, and (b) $0.25Sm_2O_3$ (Sample 2) and $0.25Sm_2O_3$ – $0.25Tm_2O_3$ samples for 648 nm emission……53

Figure 4.50 Partial Jablonski diagram for selected $0.25Sm_2O_3$ – $0.25Tm_2O_3$ sample showing possible energy transfer mechanisms for Sm^{3+} and Tm^{3+} ions under 360 nm excitation……..……54

Figure 4.51 Normalized PL spectra of the selected $0.25Sm_2O_3$ – $0.25Tm_2O_3$ sample, fitted onto the absorption profiles of Chlorophyll a and b pigments, with SRCh-a and SRCh-b indicating the degree of spectrum overlap with the respective pigments……...…55

Figure 4.52 a) Temperature-dependent PL emission spectra, b) heating-cooling cycles from 25 °C to 300 °C for the selected $0.25Sm_2O_3$ – $0.25Tm_2O_3$ sample (all stability measurements are conducted under 360 nm excitation)…….……57

Figure 4.53 Sm^{3+} and Tm^{3+} co-doped luminescent glass-based plant growth LED…….58

Figure 4.54 Experimental LED plate……...……58

Figure 4.55 Plant growth chamber (the arrows represent how the temperature within the cabinet is controlled by a motorized ventilation and fans through air circulation)…… ……..…….59

Figure 4.56 a) Emission spectra of commercial UV LED chip and $0.25Sm_2O_3$ – $0.25Tm_2O_3$ sample, b) comparison of operation stability of commercial and designed growth LEDs attached on LED plates…….……61

Figure 4.57 a) The grown lettuce under experimental and control LED plates, with experimental lettuce on the left and control lettuce on the right, and. b) group of lettuce grown under the experimental LED plate at 28th and 35th day of cultivation……61

LIST OF TABLES

Table 2.1 Lists of several luminescence kinds……10

Table 3.1 Nominal compositions of produced glass samples……15

Table 4. 1 Color coordinates, PLQY and CRI values of Sm^{3+} and Tm^{3+} co-doped glasses under 360nm excitation……55

Table 4.2 Comparison of morphological characteristics and chlorophyll content between lettuce grown in experimental and control groups……67

ABSTRACT

Samarium and Thulium Doped Luminescent Glass-Based LEDs in Indoor Agriculture Applications and Their Effects on Plant Growth

Utku EKİM

Department of Metallurgical and Materials Engineering

Master of Science Thesis

Supervisor: Assoc. Prof. Dr. Ali Erçin ERSUNDU

This study addresses the challenges of sustainable and productive agricultural practices facing climate change and the destruction of agricultural land. For this purpose, the development of a new plant-growth LED based on Sm^{3+} and Tm^{3+} added luminescent glasses with color converting properties is offered. This LED aims to increase the growth rate of plants by increasing the rate of photosynthesis and the intensity of photosynthetically active radiation (PAR) reaching crop pigments. A remarkable 56% photoluminescence quantum yield (PLQY) is produced by the designed LED, which has photoluminescence (PL) peak positions between 454 and 648 nm and spectrum coverage of 50% and 39% of the chlorophyll a and b absorption areas, respectively. Additionally, the developed plant growth LED has outstanding qualities, remaining unaffected by temperature changes and prolonged operating times. The designed LED exhibits notable improvements in plant growth characteristics, including increased plant height, weight, number of leaves, and enhanced levels of chlorophyll a and b and carotenoid content, while the root diameter is decreased, and the shoot-to-root ratio is diminished in comparison to the commercially available plant growth LED. The performance of a Sm^{3+} and Tm^{3+} co-doped luminescent glass-based plant growth LED is also compared to that of previously designed plant growth LED systems that use various luminescent materials, while also examining the effects of PLQY, PL position, and plant growing circumstances.

The findings imply that the developed LED system provides a more effective and environmentally friendly method of lighting for indoor horticulture and has important implications for supplying the rising global population's expanding want for food.

Keywords: Indoor plant growth LED, lanthanide-doped luminescent glass, chlorophyll a/b, sustainable agriculture, photosynthetically active radiation

ÖZET

Samaryum ve Tulyum Katkılı Lüminesan Cam Bazlı LED'lerin İç Mekan Tarım Uygulamalarında Kullanımları ve Bitki Gelişimine Etkileri

Utku EKİM

Metalurji ve Malzeme Mühendisliği Anabilim Dalı

Yüksek Lisans Tezi

Danışman: Doç. Dr. Ali Erçin ERSUNDU

Bu çalışma, mavi ve kırmızı ışık yayan renk dönüştürücü özelliklere sahip, dolayısıyla da fotosentez oranının ve hasat pigmentlerine ulaşan aktif radyasyon yoğunluğunun artmasına neden olan Sm^{3+} ve Tm^{3+} katkılı lüminesan camlara dayanan yeni bir bitki yetiştirme LED'inin geliştirilmesini amaçlamakta ve bu yolla iklim değişikliği ve tarım arazilerinin tahrip edilmesi sonucu ket vurulan sürdürülebilir ve verimli tarım uygulamalarına çözüm aramaktadır. Geliştirilen LED, 454-648 nm arasında değişen fotolüminesans (PL) tepe konumları sergilemekte, klorofil a ve klorofil b'nin emilim bölgelerinin sırasıyla %50 ve %39'unu spektral olarak kapsayarak %56 gibi kaydadeğer bir fotolüminesans kuantum verimi sağlamaktadır. Ayrıca, çalışma sonucunda geliştirilen bitki yetiştirme LED'i, sıcaklık döngülerinden ve uzun çalışma sürelerinden etkilenmeden stabil bir performans sergilemektedir.Bu çalışmanın ışığında aynı çevresel koşullar altındaki Roman marulları kullanılarak, piyasada bulunan bitki yetiştirme LED'i ile geliştirilen LED arasında karşılaştırmalı bir çalışma yapılmış, ve tasarlanan LED'in; bitki boyu, ağırlığı, yaprak sayısı ve gelişmiş klorofil a, klorofil b ve karotenoid içeriği seviyeleri dahil olmak üzere bitki büyüme özelliklerinde önemli gelişmeler gösterdiği, bitki kök çapının ve sürgün-kök oranının piyasada bulunan bitki yetiştirme LED'lerine

kıyasla azaldığı görülmüştür. Bu çalışma ayrıca Sm^{3+} ve Tm^{3+} katkılı lüminesans cam tabanlı bitki yetiştirme LED'inin performansını, PLQY, PL pozisyonu ve bitki yetiştirme koşullarının etkisini araştırarak, farklı lüminesans malzemeler kullanan diğer rapor edilmiş bitki büyüme LED tasarımlarıyla karşılaştırmaktadır. Sonuçlar, geliştirilen LED sisteminin iç mekan bahçeciliği için daha verimli ve sürdürülebilir bir aydınlatma yolu sunduğunu ve hızla çoğalan dünya nüfusunun artan gıda taleplerini karşılamak için önemli etkileri olduğunu göstermektedir.

Anahtar Kelimeler: İç mekan bitki büyütme LED'i, lantanit katkılı lüminesans cam, klorofil a/b, sürdürülebilir tarım, fotosentetik olarak aktif radyasyon

1
INTRODUCTION

1.1 Literature Review

The development and application of rational, efficient, and modern agricultural practices has become increasingly important in recent years due to the loss of agricultural land to development and the increasing global population. [1,2] The combustion of fossil fuels for energy has resulted in environmental degradation, particularly global warming, which has caused global temperatures to rise by 1.41 °C. This rise in global temperature is predicted to cause a 56% loss in agricultural productivity by the end of the century due to climate change. [3] Global warming is causing the rapid loss of horticultural land and weather variability, making it difficult to meet the growing food demands of the world population. Therefore, indoor horticulture and plant growth facilities have become more popular in recent years due to their many advantages over traditional outdoor farming methods. Indoor plant growth facilities can grow crops all year round, regardless of the season. This means that there is always a steady supply of food available, which is not always the case with traditional outdoor farming methods. The second benefit is that indoor plant growers have more control over the growing environment, which can lead to improved plant growth, higher yields, and better-quality crops. Thirdly, these facilities protect crops from pests, diseases, and harsh weather conditions, reducing the need for harmful pesticides and other chemical treatments. Finally, their proximity to urban centers lowers can reduce the transportation costs and carbon emissions associated with food production. In general, indoor horticulture and plant development facilities offer an efficient, sustainable, and safe alternative to conventional outdoor farming methods. [4] Therefore, increasing productivity in indoor horticultural applications through research is of utmost importance. [5]

As light is the primary energy source for plants among the several physical factors that influence their development, such as humidity, CO_2 concentration, and temperature, optimizing the right and effective use of light is essential for maximizing plant growth and development in this context. [6] Light has an impact on plants in two different ways: first, as a source of energy based on photon energy, and second, as a medium for signaling

based on heat flux, causing morphogenetic traits including plant growth and structure. [7] Photoreceptors are specialized proteins that enable plants to absorb light. Photoreceptors are categorized into two groups: (a) harvesting pigments (chlorophyll, and carotenoids), and (b) photosensory pigments. By utilizing photosynthetic energy, harvesting pigments enable the plant to produce energy, whereas photosensors control physiological reactions by activating gene groups. [8] There are two primary categories of chlorophyll: chlorophyll a and chlorophyll b. Chlorophyll a is a pigment that absorbs light in the violet-blue and orange-red portions of the spectrum between 430 and 660 nm. Chlorophyll b is an auxiliary pigment that absorbs sunlight and transfers it to chlorophyll a. It filters out light between 450 and 650 nm. [9] Red and blue light are therefore essential for the development of plants. Red light is perceived by plants and controls a number of physiological processes, including seed germination, stem lengthening, leaf expansion, and flower induction. A variety of biological processes, including stomatal opening, chloroplast movement, circadian rhythms, root development, and seedling de-etiolation, are regulated by blue light, which is also detected by plants. [7] Additionally, red and blue light, as well as their proportions, are known to have the capacity to increase the yield in photosynthesis and development on different plant growth parameters. [10] By altering the red-to-far-red ratio detected by phytochrome pigment, one of the most well-known photosensor pigments, far red light also has a significant impact on controlling plant development and growth. [7,11,12]

The unique optical and emission characteristics of inorganic photoluminescent materials are making them more and more desirable for plant growth light emitting diodes (LEDs). [13–36] Nevertheless, despite their well-suited spectral properties, their instability typically continues to be a serious obstacle. Therefore, to guarantee these photoluminescent materials' effective performance, it is typically crucial to encapsulate them in a chemically, thermally, and mechanically stable environment. Given their great chemical stability and wide range of wavelength transparency, glass encapsulants offer a viable solution for this use. Use of luminescent glass-based plant growth LEDs is thus a promising method to maximize the use of light in horticulture applications. Recently, many different studies have been reported where lanthanides [37–42], quantum dots [43–46], phosphors [47–51], transition metals [52–54], and luminescent films [55–57] are incorporated into glasses.

Due to their simple manufacture and potential for homogenous emission, lanthanides have the potential to be employed as color converters for plant growth LEDs. [53] Sm^{3+} and Tm^{3+} ions are leading examples of lanthanides that have been demonstrated to absorb in the ultraviolet (UV) region and emit with great efficiency in the blue and red region. [58] These characteristics can be used to create color-changing substances that convert UV light into beneficial blue and red light, which can improve photosynthesis and plant growth. By converting a portion of the UV region to red and blue light, it is possible to increase the daily light integral while maintaining a constant photoperiod, which can further stimulate the appropriate pigments and enhance de-etiolation, root and stem growth rate, and leaf volume. The chlorophyll pigments can be more effectively irradiated by more of these two types of photons, improving the efficiency of photosynthesis. [7]

1.2 Objective of Thesis

This study suggests a different application to boost the yield of plants produced in greenhouses as one of the measures done to enhance plant yield as a result of the world population's rapid development and the incapacity of agricultural operations to fulfill the necessary needs. The goal of this study is to examine the application of a novel Sm^{3+} and Tm^{3+} co-doped luminescent glass-based plant growth LED with color-converting capabilities that emits both blue and red light. To the best of current knowledge, there has been no prior research conducted on the co-doping of Sm^{3+} and Tm^{3+} ions in a glass host specifically for the goal of producing a plant growth LED.

1.3 Hypothesis

Comprehensive analysis reveals that lettuce plants grown under Sm^{3+} and Tm^{3+} co-doped luminescent glass-based plant growth LEDs experiences significant improvements in various growth parameters, demonstrating the potential of these LEDs to promote plant growth. Effective light absorption is achieved by carefully matching the glass composition to the absorption region of chlorophyll a/b and carotenoid. A proof-of-concept plant growth LED system is designed and applied for Romaine lettuce growth, where Sm^{3+} ions are selected due to their emission spectrum that overlaps with that of the red region of chlorophyll a/b and carotenoid absorption, while Tm^{3+} ions are chosen for their overlap in that of the blue region.

2
THEORETICAL INFORMATION

2.1 Effect of Light on Plant Growth

The world community is currently dealing with the effects of extensive reliance on fossil fuels to meet the growing energy needs, together with the alarming loss of wooded areas. This problem has resulted in significant climate changes linked to the global warming phenomenon. Over the past two centuries, there has been a noticeable increase in global temperature of 1.41°C. By the end of the 21st century, scientists [17] predicted a severe 56% decline in all agricultural production, mostly due to the combined effects of global warming, climatic fluctuations, and the widespread extinction of agricultural areas. [18] The best way to use and maximize solar radiation energy to increase agricultural productivity has been the subject of much research over a long period of time. [19] Light has two crucial roles in the complex process of plant development. First of all, it acts as a primary source of energy during photosynthesis, giving plants the fuel, they need for metabolic processes. Second, light organizes essential elements of plant growth and morphology by acting as an effective signaling agent that is closely linked to morphogenetic processes. [20]

The impact of light is the most significant factor in plant growth, and different wavelengths of light can have varied effects. In particular, red and infrared rays with comparatively less energy enhance plant growth while UV rays, which are on the left side of the energy spectrum and have relatively more energy, have the opposite effect.

The term "daylight" refers to the portion of solar energy that reaches the surface of the Earth. UV and blue light components predominate throughout the large daytime spectrum. Similar to how it affects other creatures, UV light has a variety of harmful effects on plants. Empirical studies have conclusively shown that plants exposed to high levels of UV radiation suffer substantial negative effects, including slowed stem elongation and hampered leaf formation. Additionally, a separate investigation focusing on soybean seedlings revealed disturbances in the delicate equilibrium of mineral elements within the roots, stems, and leaves, along with a discernible decrease in dry matter accumulation, which ultimately caused a significant decline in overall plant growth

and subsequent crop yield. [21] The corollary effects of UV radiation have also been proven by a plethora of scientific studies, including reduced photosynthetic efficiency, decreased biomass production, decreased protein values in plants, and consequent impairment to DNA integrity and chloroplast functionality. [22] With reference to agriculture, UV radiation is categorically recognized as an undesirable wavelength range given the substantial body of prior studies. [23] According to the scientific literature, red and orange light have a greater impact on photosynthesis and yield in plants than blue and cyan light. [24] Red light is efficiently absorbed by phytochrome pigments, which are involved in a variety of physiological processes, including plant growth and development. Inducing photosynthesis and starch accumulation through phytochrome-mediated mechanisms, elevated red light levels have a favorable effect on crop development. [25] Important findings have been made showing that red light at the ideal wavelength range strongly promotes biomass expansion in lettuce, whereas increased exposure to UV and blue light inhibits germination and leaf expansion, thereby impairing overall plant growth. [26-27] Red light is widely used for growing lettuce and other green vegetables, according to earlier studies. Modern greenhouse techniques produce beneficial results when red light is combined with a certain amount of blue light. For instance, a study [28] has shown that 640 nm red light combined with blue light increases carbohydrate and antioxidant levels while simultaneously decreasing unfavorable nitrate concentration. It should be noted that this effect is more pronounced in plants with green foliage than in those with red foliage. [29] These results were supported by a study done on parsley and dill, which showed that the addition of red light caused a noticeable increase in phenolic compounds, vitamin C, and carbohydrate content, concurrently leading to a rapid reduction in accumulated nitrate levels. Numerous studies have looked at the proportions of blue and red light in the scientific literature, particularly in relation to photosynthetic efficiency. According to two independent studies [30-31], an increase in the amount of blue light enhances the nutritional quality and antioxidant content of green vegetables while concurrently lowering nitrate levels. Similar studies focused on red lettuce by various research teams have shown that higher levels of blue light cause increased pigmentation, indicating that a short period of supplementation with blue light is sufficient to produce the desired effects in production settings. [32-33] Additionally, blue light displayed similar features to red light by favorably impacting morphological traits like plant development and leaf expansion in tests on red plants where the beneficial effects of red light were comparably less prominent. [34] According to an experiment,

blue light stimulates the cryptochrome system, enabling proper interactions between the pigments chlorophyll and carotenoids, which in turn promotes increased plant growth, photosynthesis, and antioxidant levels. These studies highlight the important effects of blue light on green vegetable growth, photosynthesis, and antioxidant systems. In another study, blue light was found to greatly increase overall efficiency even though red light is an excellent regulator of photosynthesis. [35]

Photoreceptors are specialized proteins that enable plants to absorb light. Chlorophyll and carotenoids, which are used in photosynthesis, are categorized into two groups: photosensory pigments and pigments used in photoreceptors. By utilizing photosynthetic energy, harvesting pigments enable the plant to produce energy, whereas photosensors control physiological responses by activating gene groups. [8] The two main types of chlorophyll are chlorophyll a and chlorophyll b. Chlorophyll A is a pigment that absorbs light between 430 and 660 nm in the violet-blue and orange-red regions of the spectrum. An auxiliary pigment called chlorophyll b absorbs sunlight and sends it to chlorophyll a. It blocks light with a wavelength of 450 to 650 nm. [9] Red and blue light are therefore essential for the development of plants. Red light is perceived by plants and controls a number of physiological processes, including seed germination, stem lengthening, leaf expansion, and flower induction. Biological processes like stomatal opening, chloroplast movement, circadian rhythms, root development, and seedling de-etiolation are all regulated by blue light, which is also detected by plants. [7] Additionally, red and blue light ratios are proven to have the power to boost photosynthetic production and development on several plant growth parameters. [10] On the other hand, phytochrome pigment, one of the most well-known photosensor pigments, senses the red to far red ratio, which is vital for controlling plant development and growth. [7,11,12]

2.2 Light Management in Greenhouses

Light is currently the most crucial element in the growth of plants cultivated in greenhouses, hence it is crucial that greenhouses are properly and adequately illuminated. The total amount of light that is received over the course of a day is represented by the Daily Light Integral (DLI). The DLI counts the number of photons in moles (mol) that impact on a square meter of surface area (m^2) over the course of one day (d), expressed as $molm^2d^1$. It has been discovered that increasing the DLI improves the quality of the majority of ornamental crops and the production of the majority of vegetable crops in controlled conditions like greenhouses. Since the DLI value varies according to the

amount of seasonal light that plants receive, the levels of DLI for plants in greenhouses should be adjusted accordingly.

Utilizing roof materials with high light transmittance is the most popular technique for modifying the DLI value in greenhouses. Glass or translucent plastic are therefore frequently used as roof materials. After an extended period of exposure to strong sunshine, plastic materials are more susceptible to some amount of degradation. The selection of glass materials for roof coverings is so crucial. The number of additional measures needed to modify the DLI value can be reduced in half in greenhouses using these highly transparent glass materials.

Installing supplemental lighting within the greenhouse is another frequent technique used to change the DLI value in greenhouses. Even when highly transparent materials are used as roof coverings, there may be instances in certain locations where the amount of incoming sunlight is insufficient for the intended growth of the planted plants. Additional illumination systems, including LEDs and plant growth lamps, are therefore required. [59]

Pereira et al. reported that six key categories of photoperiod, period, dawn phase, light intensity (amplitude), light offset, and duration of twilight were used to assess the impact of light on plant development. As the photoperiod rose, it was discovered that flower development was, to a certain extent, accelerated. However, when these six variables were considered collectively, problems emerged, including a considerable increase in energy use in the trial carried out with supplemental lighting. [60]

2.2.1 The Importance of Shading Applications in Greenhouses

While some plant species show a high tolerance to light, many others are sensitive to too much light. As a result, it is crucial to use new techniques in greenhouse settings that support these light-sensitive plants. Similar to this, greenhouses located in certain areas may be vulnerable to excessive sunlight. The employment of shade systems within greenhouse operations becomes crucial in order to mitigate these concerns. In addition to regulating the complex interactions between plants and light, shading makes it easier to maintain ideal thermal conditions inside of the structures. External and internal techniques can be used to classify strategies for reducing excessive light in greenhouses. In order to successfully shade an area, it is essential to choose greenhouse roofing materials that have light-absorbing qualities. This will reduce the amount of irradiance

entering the area. Additionally, the use of internal systems, such as misting mechanisms, helps to manage and control the current temperature levels within the greenhouse environment. [61]

Krieger et al. reported that, intermittent shadowing of plants caused their chlorophyll a and b concentrations to increase and surpass those of plants that did not receive any shading. The study also revealed the significant influence of light interaction on the nutritional composition of plants. Krieger et al. discovered that, plants with the appropriate timing of shading have decrease in the prevalence of parasite species. [62]

In addition, shade becomes crucial for low-light crops and specific uses such root cutting propagation in order to limit the overall intake of solar radiation. By absorbing and reflecting incident solar energy before it enters the enclosed greenhouse, external shading techniques have the advantage of reducing the heating effect on the surrounding air and enclosed objects.

2.2.2 Indoor Horticulture Applications

Meeting the food needs of the expanding global population is challenging due to the fast loss of horticulture areas and meteorological variability brought on by global warming. [3] Because they have so many advantages over traditional outdoor farming techniques, indoor horticulture and plant development facilities have become increasingly popular in recent years. There are many advantages brought by agricultural practices carried out indoors. First of all, these facilities enable the year-round production of crops, eliminating the dependency on seasonal variations and ensuring a constant supply of food. The second advantage is that growers have better control over the environmental factors, which optimizes plant development and increases agricultural yields with higher quality. Thirdly, these buildings shield crops from toxic pesticides and other chemical treatments by shielding them from illnesses, harsh weather, and pests. Finally, the cost of transportation and the carbon footprint of food production are reduced by their closeness to urban areas. The future of agriculture depends on indoor horticulture and plant growth facilities because they offer efficient and environmentally friendly alternatives to traditional outdoor farming methods. [4] Therefore, it is crucial to conduct research to increase productivity in indoor horticulture applications. [5]

Practices for indoor farming are developing and spreading more widely. Lighting solutions that simulate sunshine must be used in indoor horticulture applications in order

to support and improve plant development. Commercial red and purple plant lamps, as well as LED lighting systems for plant development, are some of the lighting systems most frequently utilized in indoor horticulture applications. In addition to being commonplace in our daily lives, LED lighting solutions are now also essential in agricultural applications. As materials and radiation capabilities advance, more research is being done on LED lights that primarily generate red light. [63]

Inorganic luminescent compounds are employed as a source of red radiation in red LED lights. These inorganic luminescent materials, which emit a lot of radiation, are very effective at providing plants the Daily Light Integral (DLI) they require to develop. [13–36] However, the issue of degradation, which is reliant on temperature and environmental factors, limits the deployment of LEDs using inorganic phosphors despite their ongoing development and rising ubiquity. [64,65,66]

2.3 Luminescence

Luminescence, commonly referred to as "cold light," is a word used to describe a variety of processes in which a substance emits electromagnetic waves (light) without being heated up, i.e., the emission is not thermal radiation. Incandescence, or the light produced by a heated tungsten filament in a conventional light bulb, is the term for the light that results from heating something up. The luminescence event is basically based on energy transfers between atoms. This can be briefly explained as follows: The electrons of an atom that are in a stable state (also known as the ground state) can be stimulated and migrate to higher energy levels by absorbing a photon. The amount of energy that one electron can absorb to advance to a higher level is significant for each of the 10 atoms and their electrons. The electrons, however, tend to return to their ground state after becoming excited since they cannot remain in an excited state for a very long time. When an electron returns to the ground state, it emits light that has energy exactly equal to the energy difference between its stable and excited states. [67-69] This energy's quantity can be determined using the equation that follows [70]:

$$\mathrm{E} = \frac{hc}{\lambda} \tag{2.1}$$

2.3.1 Luminescence Types

Depending on the excitation method, luminescence is divided into various categories. Bioluminescence, chemiluminescence, electroluminescence, and photoluminescence are some examples of luminescence types. In Table 2.1, list of several luminescence types are given with their definitions and applications.

Table 2.1 Lists of several luminescence kinds [71]

Phenomenon	Definition	Applications
Photoluminescence	It is a procedure by which any substance, upon photon absorption, emits light.	Fluorescent lamps and display devices
Radioluminescence	Ionizing radiation causes a substance to emit light, which is what happens in this situation.	X-ray imaging, scintillation
Electroluminescence	It is a phenomenon where a semiconductor emits light as a result of an electrical current or powerful electric field.	LEDs, laser diodes
Chemiluminescence	Chemical reactions usually generate excited intermediates that emit light when they decay back to their ground states.	Chemical analysis
Thermoluminescence	When heat reaches a critical threshold in some crystalline materials, a phenomenon called luminescence occurs in which the material releases light that it had previously absorbed from ionizing radiation or electromagnetic radiation.	Dosimetry of ionizing radiation
Mechanoluminescence	This kind of light is produced by the deformation of solids, elastic deformation, and plastic deformation.	Piezoelectric materials

2.3.2 Photoluminescence

One of the numerous types of luminescence is photoluminescence (PL), in which light emission occurs after a substance has been energized by photons. Fluorescence and phosphorescence are two subtypes of photoluminescence. The length of time it takes to do so is the main distinction between them. Fluorescence and phosphorescence have a variety of definitions, but the most basic is that fluorescence is the production of light right after photoexcitation and that the emission ends quickly if the stimulation source is removed. In contrast, phosphorescence emission lasts longer after the excitation source is

removed. Because there is an intermediate level called the metastable level or electron trap between the excited and ground states in which a transition from this level to lower levels is prohibited, phosphorescence takes longer to occur. After entering an electron trap from an excited state, an electron stays there until it undergoes a forbidden transition or becomes excited again. The duration of the electron trap determines how much radiation is emitted during phosphorescence. [72, 73] To put it simply, phosphorescence occurs when light persists after the source has been removed, while fluorescence disappears instantly.

2.3.3 Energy Transfer Mechanisms

When exposed to a bright enough light source, trivalent Ln^{3+} ions release photons across the entire electromagnetic spectrum, from the UV to the near infrared and beyond. The three primary photoluminescence (PL) mechanisms that take place in Ln^{3+} doped luminescent materials are shown in Figure 2.1 downshifting (DS), down-conversion (QC), also known as quantum cutting, and up conversion (UC). We refer to the UC process as an "anti-Stokes" process because it violates the Stokes law. [74]

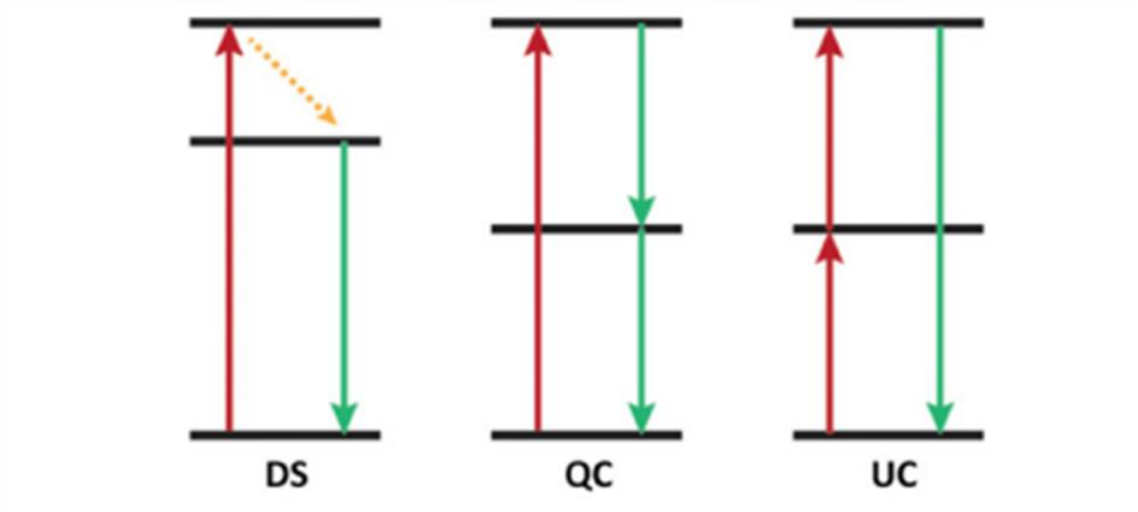


Figure 2.1 The three energy transfer processes [88].

Down-shifting (DS) and quantum cutting (QC) processes: The processes of downshifting (DS) and quantum chopping (QC) are distinct yet connected. During DS luminescence in Ln^{3+}, a high-energy photon is absorbed and transformed into a low-energy photon by a Stokes mechanism. QC will result in quantum values greater than unity if the absorbed photon decays into two or more photons of lower energy. [75] Dexter proposed in 1957 the idea of splitting a single photon into two photons with lower energy in order to achieve

quantum yields greater than 100%. Later, in 1974, Sommerdijk et al. demonstrated that in the hosts YF_4 and $NaYF_4$, a single UV photon of Pr^{3+} (210 nm) can be split into two visible photons. In a study by Piper et al., who used a Pr^{3+} activated phosphorus material, quantum yields greater than one was also observed. [76] One frequent use of the QC is to boost solar cells' efficiency.

2.4 Photoluminescent Materials Used in LEDs

LEDs are made of photoluminescent materials, which evolve along with technology and are replaced by newer, more advanced materials. The components utilized as luminescent color changers evolve as technology advances. Synthetic paints with phosphor- and epoxy-based bases were used as examples in the first luminescent color converters. These phosphor-based luminescent color converters are often sprayed to surfaces or employed in sandwich structures with another silicone or organic substrate. [77] However, due to the poor correlated color temperature (CCT) and color rendering index (CRI) values of phosphor materials as well as their low thermal and structural stability, researchers have looked for alternate architectures for luminous color converters. [64-66] In order to increase the stability of the phosphor structure, research has now concentrated on synthesizing phosphor structures inside of a glass matrix that acts as insulation from the outside environment. The development of Phosphor in Glass (PiG) structures is the product of these efforts. Although this method increases thermal stability, PiG demonstrates inadequate ability to convert colors into luminous ones and has problems with reaction formation between the glass matrix and the phosphor material, among other things. [78] Further study has shown that transition metals [52–54] and quantum dots [43–46] can also be used as luminous substances. Quantum dots can be affected by environmental variables like temperature, humidity, and air conditions, but they are also prone to degradation, just like phosphor materials. [79] The most popular investigations lately have often centered on luminous lanthanide materials. Their field of applications has been broadened by their high emission intensities and quantum yields. Additionally, these materials have been synthesized within glass matrices in the research because of their susceptibility to environmental degradation. [37–42]

2.4.1 Lanthanide-doped Luminescent Glasses

Currently, glass materials have become the excellent choice for encapsulating luminescent materials due to their superior thermal, chemical, and mechanical durability,

adaptable optical properties, straightforward manufacturing processes, and capacity to neutralize toxic elements up to acceptable levels. [38,39] As encapsulant glass materials, silica, germanate, borosilicate, and tellurite glasses are usually used. [64,66,79] In comparison to crystals and powders, glass hosts are simple to make and have a higher solubility for lanthanides and quantum dots. Additionally, glasses can be produced in bulk, powder, and fiber forms and have strong optical transmission over a wide spectrum of wavelengths. [80-82]

Inorganic glass networks with excellent thermal stability, a low thermal expansion coefficient, high softening temperatures, melting at low temperatures, and improved corrosion resistance can be created by combining B_2O_3 with SiO_2 elements. Borosilicate glasses can be used to shift colors and withstand environmental variables due to their great properties. [81,82]

2.4.2 Agricultural Applications for Lanthanide-Doped Glass-Based LEDs

Natural light in the 400–700 nm range, commonly referred to as photosynthetically active radiation (PAR), has been the main source for these essential processes throughout the evolution of plants. Plants have therefore developed systems to make the best use of this light spectrum. For instance, stomata control crucial environmental exchanges like CO_2 and humidity permeability. It is important to keep in mind, nevertheless, that exposure to UV radiation with wavelengths below 400 nm might stress plants, impairing growth and developmental processes. [83].

Due to its straightforward manufacture and capacity for homogenous emission, lanthanides doped glass materials have the potential to be employed as color converters for LEDs that support plant development [83]. The lanthanide ions Sm^{3+} and Tm^{3+} are leading examples of compounds that have been demonstrated to absorb in the UV area and emit with high efficiency in the blue and red range [84]. Utilizing these characteristics, color-changing materials can be created that turn UV light into beneficial blue and red light, which can improve photosynthesis and plant growth.

It is feasible to raise the daily light integral while maintaining a constant photoperiod by converting a portion of the UV area to red and blue light. This can further stimulate the necessary pigments and improve de-etiolation, root and stem development rate, and leaf volume. The chlorophyll pigments can be more effectively irradiated by more of these two types of photons, improving the efficiency of photosynthesis [85].

3
EXPERIMENTAL STUDIES

3.1 Sample Synthesis

Using a traditional melt-quenching method, seven distinct luminescent glass samples were produced. The analytical reagent grade (>99.9%) raw ingredients, including Na_2CO_3, $CaCO_3$, Al_2O_3, H_3BO_3, SiO_2, Sm_2O_3, and Tm_2O_3, are provided by Sigma-Aldrich and Alfa Aesar and used without additional purification. The nominal glass composition is $15Na_2O$-$20CaO$-$5Al_2O_3$-$15B_2O_3$-$45SiO_2$ with varied mol% of xSm_2O_3 and yTm_2O_3 (x and y = 0.125, 0.25, and 0.5). Table 3.1 provides a thorough summary of the chemical composition of the samples along with their names.

Table 3.1 Nominal compositions of produced glass samples

Sample name	Nominal Composition (mol %)					
	SiO_2	Na_2O	Al_2O_3	B_2O_3	Sm_2O_3	Tm_2O_3
$0.125Sm_2O_3 – 0.125Tm_2O_3$	45	15	5	15	0.125	0.125
$0.125Sm_2O_3 – 0.25Tm_2O_3$	45	15	5	15	0.125	0.25
$0.25Sm_2O_3 – 0.125Tm_2O_3$	45	15	5	15	0.25	0.125
$0.25Sm_2O_3 – 0.25Tm_2O_3$	45	15	5	15	0.25	0.25
$0.50Sm_2O_3 – 0.50Tm_2O_3$	45	15	5	15	0.50	0.50
$0.25Sm_2O_3$	45	15	5	15	0.25	-
$0.25Tm_2O_3$	45	15	5	15	-	0.25

The raw materials are combined and ground to fine powder using an agate mortar and pestle after being precisely weighed using high-precision scales (10^{-4} g) (see Figure 3.1).

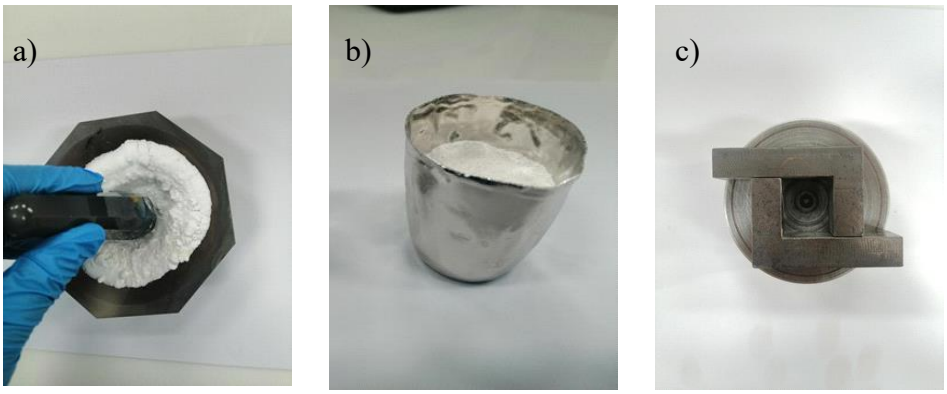


Figure 3.1 a) Glass batch homogenization in agate mortar, b) glass batches in platinum crucibles, c) steel mold that glass poured

The resulting mixture is melted in platinum crucibles for two hours at 1200 °C under air atmosphere using Protherm Box Furnace. while being stirred occasionally to prevent bubble formation and guarantee homogeneity. Following this, the melts are poured into stainless steel molds that have been preheated, pressed by steel plates (Figure 3.1c). In order to relieve internal stresses brought on by rapid cooling, the poured glass samples immediately placed in pre-heated Nabertherm Box muffle furnacebelow their glass transition temperature at 400°C for 5 h and cooled to room temperature inside the muffle furnace. After heat treatment process, to achieve high-quality surfaces ideal for optical characterization tests, the samples are then ground and polished to a thickness of 2.5 mm using a Struers LaboPol-20 Grinder Polisher machine with different sizes of sandpapers (120, 320, 800, 1200, and 2500 mesh) and 1μ polishing pad. As a result, synthesized samples are coded based on the mol% of Sm_2O_3 and Tm_2O_3 content, for example, $0.25Sm_2O_3$ - $0.25Tm_2O_3$. For all samples examined in this study, glass synthesis methods and conditions were kept constant.

3.2 Sample Characterization

3.2.1 Structural Analysis

The Malvern PANalytical Empyrean Multicore High-Performance X-ray Diffractometer (XRD) with an average wavelength of Cu Kα1 and Cu Kα2 radiation (λ=0.15418 nm, voltage: 45 kV, current: 40 mA) is employed to identify the amorphous nature of the as-cast samples in the 2θ range from 10° to 90° with a scanning step size of 0.02°.

3.2.2 Thermal Analysis

To examine the thermal behavior of the as-cast materials, thermal analysis measurements are made using a Netzsch STA 449 F3 Jupiter instrument. To find the glass transition (T_g) temperature, a chosen powdered sample weighing 30 mg is heated in a platinum pan at a rate of 10 °C/min while being surrounded by a nitrogen environment.

3.2.3 Optical Analysis

Using an Edinburgh DS5 UV-Vis spectrophotometer with a resolution of 0.5 nm and a wavelength range of 190 to 1100 nm, the optical absorption spectra of the samples are measured.

3.2.4 Photoluminescent Analysis

Using an Edinburgh Instruments FS5 fluorescence spectrophotometer with a 150W xenon lamp as the excitation source, photoluminescence (PL) measurements are performed. The PL quantum yield (PLQY) measurements are conducted in an integrated sphere (150 mm internal spherical cavity, polytetrafluoroethylene coated) under 360 nm excitation wavelength with a signal to noise ratio of water Raman signal greater than 6000:1 and 0.5 nm spectral resolution. The PLQY is evaluated using the following equation with an estimated error rate of ± 5%:

$$\boldsymbol{PLQY = \frac{number\ of\ emitted\ photons}{number\ of\ absorbed\ photons} = \frac{L_{sample}}{E_{reference} - E_{sample}}} \qquad (3.1)$$

where $E_{reference}$ and E_{sample} are, respectively, the reference and sample's relative scattering intensities of excitation light that wasn't absorbed. The emission intensity, L_{sample}, is calculated by integrating the region beneath calibrated emission spectra. The quantity of photons absorbed is determined by the variation in scattering integrated areas between the reference and sample.

The Edinburg FS5 Spectrofluorometer, which uses a time-correlated single-photon counting (TCSPC) method with a microsecond xenon lamp as the excitation source at 360 nm, is used to measure time-resolved lifespan spectra. The recorded decay curves are fitted using a bi-exponential equation to obtain the converging $\chi 2$ values to unity as indicated below:

$$I(t) = A_1 e^{\left(\frac{-t}{\tau_1}\right)} + A_2 e^{\left(\frac{-t}{\tau_2}\right)} \qquad (3.2)$$

where, $I(t)$ is emission intensity, τ_1 and τ_2 are the lifetime numerical values, and A_1 and A_2 are decay constants. Average lifetime value of each transition is calculated by using the following expression:

$$\tau_{meas} = \frac{A_1\tau_1{}^2 + A_2\tau_2{}^2}{A_1\tau_1 + A_2\tau_2} \quad (3.3)$$

In order to evaluate the thermal resistance of the glasses, temperature is increased from 25 °C to 300 °C over the course of up to five heating and cooling cycles. Temperature-dependent PL measurements are then performed using a heated solid transmission attachment from Pike Technologies installed in the spectrofluorometer.

3.2.5 Color Properties

Using the OSRAM Color Calculator program, PL emission spectra of samples are used to calculate colorimetric features like CIE (1931) color coordinates and CRI (color rendering index). Using up-conversion emission data obtained through photoluminescence analysis and the following equations, the International Commission on Illumination (CIE) 1931 chromaticity coordinates were calculated in order to show the true color of the emissions.

$$x = X/(X + Y + Z) \quad (3.4)$$

$$y = Y/(X + Y + Z) \quad (3.5)$$

$$z = Z/(X + Y + Z) \quad (3.6)$$

The three tristimulus values X, Y and Z represents the three main colors of red, green, and blue, respectively and can be determined using equations given below:

$$X = \int_{400}^{700} P(\lambda)\bar{x}(\lambda)\, d\lambda \quad (3.7)$$

$$Y = \int_{400}^{700} P(\lambda)\bar{y}(\lambda)\, d\lambda \quad (3.8)$$

$$Z = \int_{400}^{700} P(\lambda)\bar{z}(\lambda)\, d\lambda \quad (3.9)$$

where λ is wavelength of monochromatic color of light, $P(\lambda)$ is spectral power distribution and x, y and z are color-matching functions. Using the Color Calculator application created by German lighting manufacturer OSRAM, sample CRI values are calculated.

3.3 Plant Tests

The experimental plant species for the plant experiments is lettuce, specifically Lactuca sativa L. cv. 'Romanie'. The seeds are first planted one by one in plastic germination trays that have been pre-filled with sponge cube blocks and tap water. As soon as the second leaf develops, the seedlings are transferred to a plant growth chamber with controlled environmental conditions. The plants are kept alive in ideal conditions for growth, which include a temperature range of 23°C during the day and 21°C at night, a relative humidity range of 65-70%, and an ambient CO_2 partial pressure. With a density of about 16 plants/m^2, the plants are grown in a particular kind of plant peat and kept in the best possible environmental conditions. The cultivation frames in the growth chamber are divided into two equal portions by a black-and-white plastic film with dimensions of 2 m x 1.2 m x 1.2 m (length, width, and height). A total of 0.72 m^2 was covered by each plant component, which measures 0.6 m x 1.2 m. Two flowerpots are placed at each part, and each flowerpot has six plants. Seedlings of lettuce are sown at intervals of 20 cm. One of the parts is selected to act as the control group and the other as the experimental group based on the lighting conditions. The growth chamber is equipped with a motorized ventilation fan (2250 rpm, 30 W, 0.13 A, maximum flow 360 m^3/h) to provide consistent airflow and lessen any potential effects of environmental variability on plant development. Fans on the sides of the cabinet assist in bringing in fresh, cool air when the LED lights inside the cabinet generate heat, and a motorized ventilation system expels the warm air from the cabinet. Irrigation is carried out regularly to meet the plants' water requirements. The growing circumstances of the plants are closely watched and managed in order to ensure consistency of results and minimize unnecessary fluctuation.

Plant height, fresh weight (FW), dry weight (DW) of shoots and roots, stem diameter, leaf number and the ratio of shoot and root (S/R) are measured at 35 days after sowing as the mean of six for each group. S/R is determined from shoot/root dry weight. Drying the samples for 40 hours at 60 °C is how the dry weight of the samples is calculated. Chlorophyll a, chlorophyll b, and carotenoids are determined using fresh lettuce samples. Fresh samples of mature lettuce leaves weighing a total of 0.2 g are pulverized in a mortar for this purpose. Once the leaf turns white, the ground is once again filtered after being submerged in 80% acetone. The filtrates are collected and diluted to a final volume of 100 mL using distilled water. The extraction's absorbance is then measured using an Edinburgh Instruments DS5 UV-Vis spectrophotometer at wavelengths of 663 nm, 645

nm, and 470 nm. The concentrations of chlorophyll a, chlorophyll b, and carotenoids are calculated using the following equations, respectively [86]:

$$Chl\ a\ \left(\frac{mg}{g}\right) = \frac{(12.72 \times OD_{663} - 2.59\ \times\ OD_{645})V}{1000W} \tag{3.10}$$

$$Chl\ b\ \left(\frac{mg}{g}\right) = \frac{(22.88 \times OD_{645} - 4.67\ \times\ OD_{663})V}{1000W} \tag{3.11}$$

$$Car\ \left(\frac{mg}{g}\right) = \frac{((1000 \times OD_{470} - 3.27 \times Chla - 104\ \times Chl\ b)\ /\ 229)V}{1000W} \tag{3.12}$$

where, Chl a is chlorophyll a, Chl b is chlorophyll b, Car is carotenoid, V is the total volume of acetone extract (mL), and W is the fresh weight (g) of the sample.

The chlorophyll absorption and the spectrum overlap degree ($SR_{chlorophyll}$) is calculated according to the following equation [87]:

$$SR_{chlorophyll} = \frac{\int P(\lambda)d\lambda}{\int P_{chlorophyll}(\lambda)d\lambda} \times 100 \tag{3.13}$$

where $P_{chlorophyll}$ (λ) is the power distribution of the absorption spectrum and λ is the wavelength, while P(λ) is calculated using the following conditions:

$$P(\lambda) = \alpha P_l(\lambda)\ \ if\ P_{chlorophyll}(\lambda) > \alpha P_l(\lambda) \tag{3.14}$$

$$P(\lambda) = P_{chlorophyll}(\lambda)\ \ if\ P_{chlorophyll}(\lambda) \leq \alpha P_l(\lambda) \tag{3.15}$$

Here P_l (λ) is the entire power spectrum of the constructed plant growth LED device and α is an arbitrary normalization constant and defined as follows:

$$\alpha = \frac{\int P_{chlorophyll}(\lambda)d\lambda}{\int P_l(\lambda)d\lambda} \tag{3.16}$$

4
RESULTS

4.1 Results

In this section, findings of all characterization studies, comprising structural, thermal, optical, and photoluminescence analyses along with sample morphologies and CIE color coordinates, are presented in detail. As a result, each sample's individual analysis is gathered and thoroughly explained for comparison.

4.1.1 $0.125Sm_2O_3 – 0.125Tm_2O_3$ Glass Sample

$0.125Sm_2O_3 – 0.125Tm_2O_3$ glass sample is synthesized by traditional melt-quenching technique. The glass composition of this sample is 15% Na_2O, 20% CaO, %5 Al_2O_3, %15 B_2O_3, %45 SiO_2, %$0.125Sm_2O_3$ and %$0.125Tm_2O_3$. The macro picture of fully transparent $0.125Sm_2O_3 – 0.125Tm_2O_3$ sample is given in Figure 4.1.



Figure 4.1 Macro picture of $0.125Sm_2O_3 – 0.125Tm_2O_3$ sample

In Figure 4.2, amorphous nature of synthesized $0.125Sm_2O_3 – 0.125Tm_2O_3$ sample is confirmed by the XRD pattern with no visible crystallization peaks.

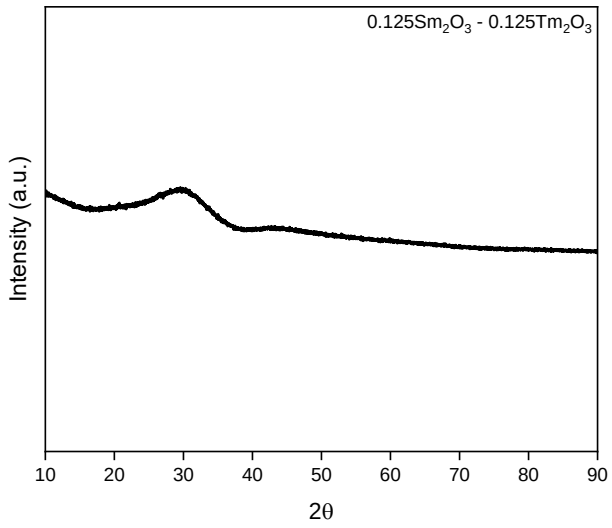


Figure 4.2 XRD pattern of $0.125Sm_2O_3 – 0.125Tm_2O_3$ sample

The thermal properties of synthesized $0.125Sm_2O_3 – 0.125Tm_2O_3$ sample were investigated with simultaneous thermal analysis (STA) and thermogram is given in Figure 4.3. The glass transition onset (T_g) of $0.125Sm_2O_3 – 0.125Tm_2O_3$ sample is detected as 564 °C.

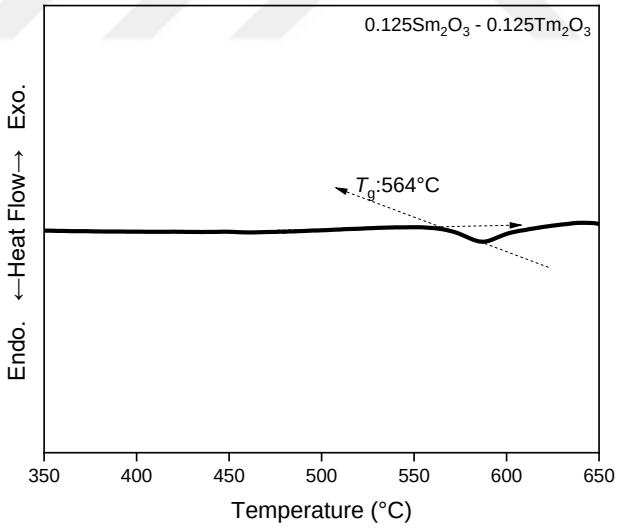


Figure 4.3 STA analysis of $0.125Sm_2O_3 – 0.125Tm_2O_3$ sample

Figure 4.4 presents the optical absorption spectrum of $0.125Sm_2O_3 – 0.125Tm_2O_3$ sample in the 190-1100 nm range. Nine distinct absorption peaks can be seen in the optical absorption spectra, six of which are located at 360, 374, 402, 473, 941, and 1072 nm and are associated with the transitions of Sm^{3+}'s $^6H_{5/2}$ to $^4D_{3/2}$, $^6H_{5/2}$ to $^6P_{7/2}$, $^4L1_{3/2}$, $^4I_{11/2}$, $^6H_{5/2}$ to $^6F_{11/2}$, and $^6H_{5/2}$ to $^6F_{9/2}$, respectively. In addition, three peaks are seen at wavelengths

of 463, 683, and 790 nm, which correspond to the transitions of Tm^{3+} from $^3H_6$ to $^1G_4$, $^3H_6$ to $^3F_3$, and $^3H_6$ to $^3H_4$, respectively.

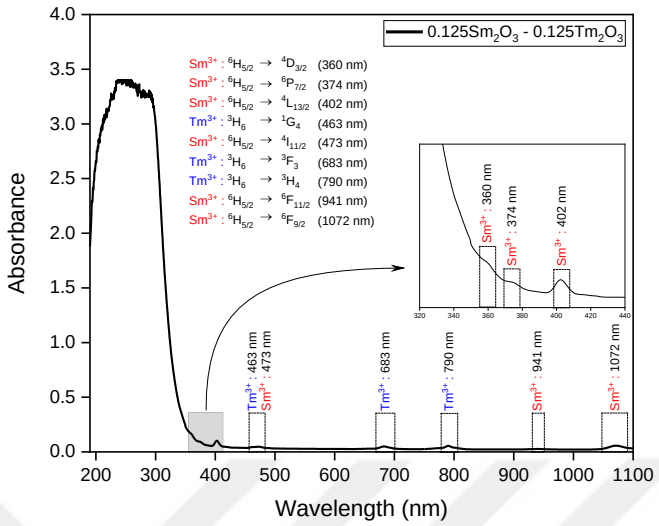


Figure 4.4 Optical absorption spectrum of $0.125Sm_2O_3 – 0.125Tm_2O_3$ sample

The excitation spectra of the $0.125Sm_2O_3$ - $0.125Tm_2O_3$ sample are shown in Figure 4.5. They were obtained through measuring the emission wavelengths at 454, 565, 602, 648, and 707 nm in the 320-420 nm excitation range, respectively.

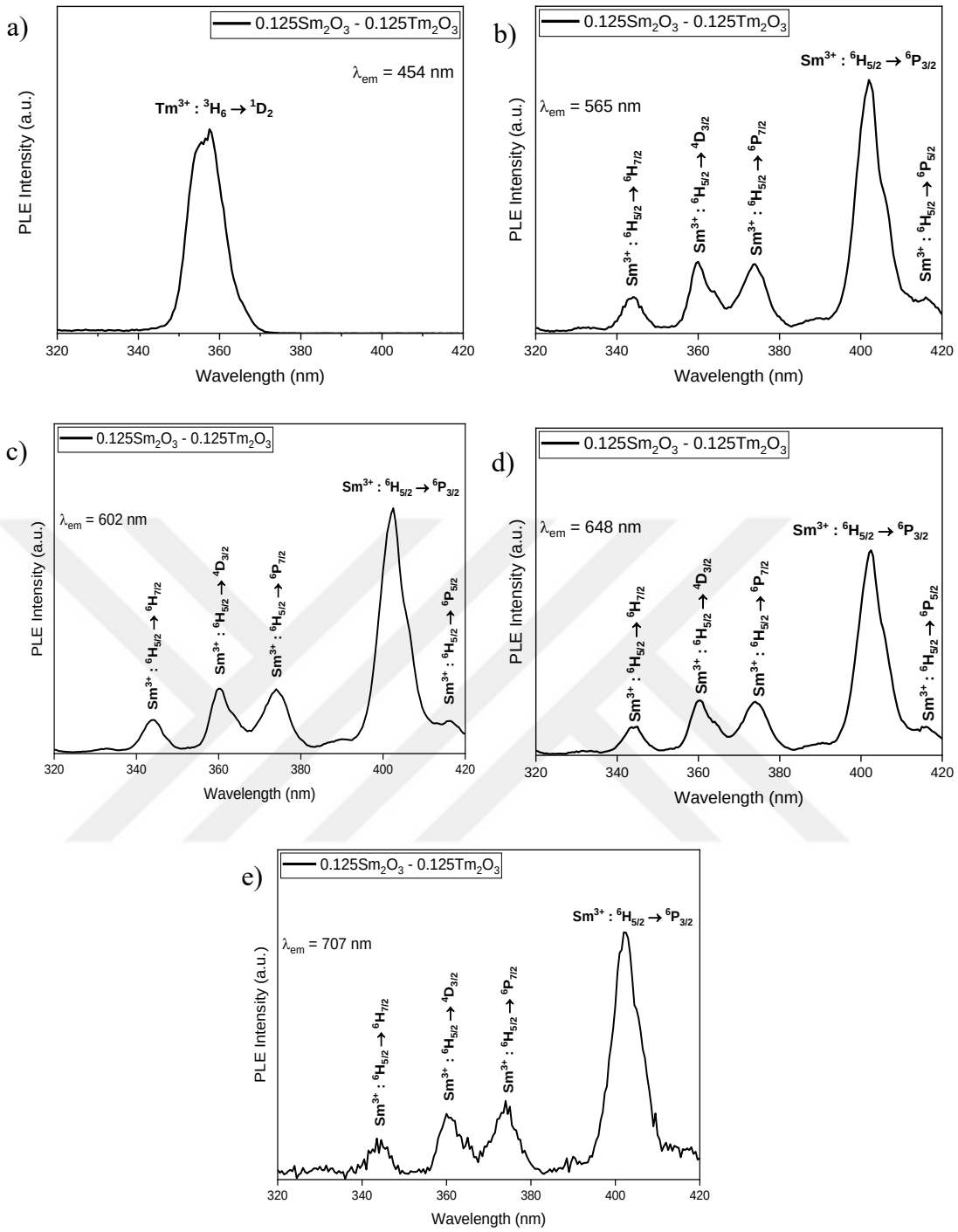


Figure 4.5 PL excitation spectra for different emission wavelengths of $0.125Sm_2O_3$ – $0.125Tm_2O_3$ sample

The PL spectra for the sample of $0.125Sm_2O_3$ and $0.125Tm_2O_3$ are shown in Figure 4.6. Six separate peaks linked to Sm^{3+} and Tm^{3+} ions are seen under 360 nm excitation. Sm^{3+} and Tm^{3+} ions emit light at 454 and 482 nm as a result of the transitions $^1D_2$ to $^3F_4$ and $^1G_4$ to $^3H_6$, respectively, whereas Sm^{3+} ions emit four spectral lines at 565, 602, 648, and 707 nm as a result of the transitions $^4G_{5/2}$ to ^6H_J (J = 5/2, 7/2, 9/2, and 11/2), respectively.

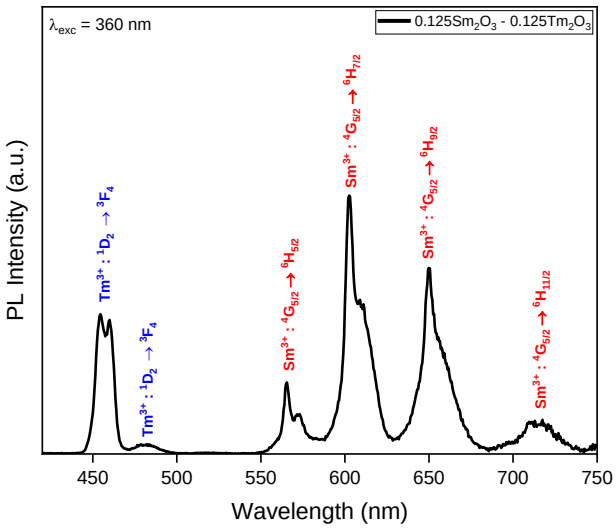


Figure 4.6 PL emission spectra of $0.125Sm_2O_3 – 0.125Tm_2O_3$ sample under 360 nm excitation

The macro picture of fully transparent $0.125Sm_2O_3 – 0.125Tm_2O_3$ sample under 360 nm excitation is given in Figure 4.7. Red emission of Sm_2O_3 ions can be seen with naked eye clearly through 360 nm excitation.

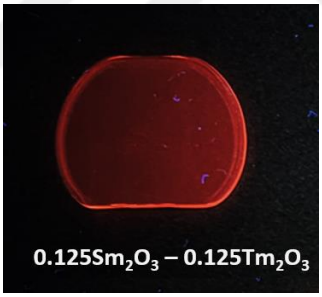


Figure 4.7 Macro photo of $0.125Sm_2O_3 – 0.125Tm_2O_3$ sample under 360 nm excitation

Figure 4.8 displays the $0.125Sm_2O_3$ - $0.125Tm_2O_3$ sample's CIE color coordinates. Using the OSRAM color calculator tool, the color coordinates (x= 0.4781, y= 0.2730) and CRI value of 33 were determined.

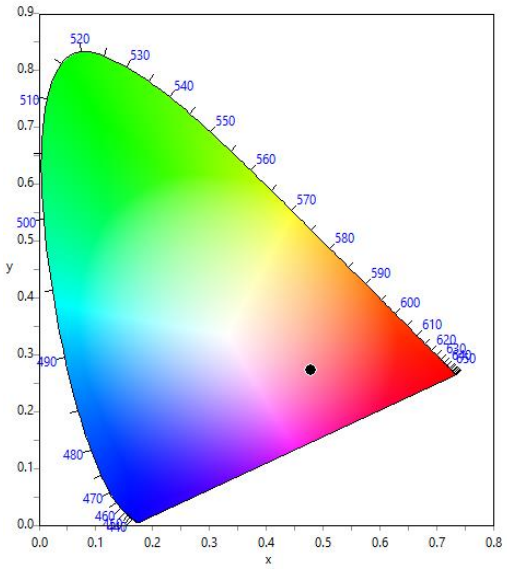


Figure 4.8 CIE color coordinates of $0.125Sm_2O_3 – 0.125Tm_2O_3$ sample under 360 nm excitation

4.1.2 $0.125Sm_2O_3 – 0.25Tm_2O_3$ Glass Sample

A glass sample coded with $0.125Sm_2O_3 – 0.25Tm_2O_3$ was produced by traditional melt-quenching technique. This sample's glass has the following composition: 15% Na_2O, 20% CaO, %5 Al_2O_3, %15 B_2O_3, %45 SiO_2, %$0.125Sm_2O_3$ and %$0.25Tm_2O_3$. Figure 4.9 shows the macro image of completely transparent $0.125Sm_2O_3 – 0.125Tm_2O_3$ sample.



Figure 4.9 Macro picture of $0.125Sm_2O_3 – 0.25Tm_2O_3$ sample

The synthesized $0.125Sm_2O_3 – 0.25Tm_2O_3$ sample's amorphous nature is supported by the XRD pattern In Figure 4.10, which shows no visible crystallization peaks.

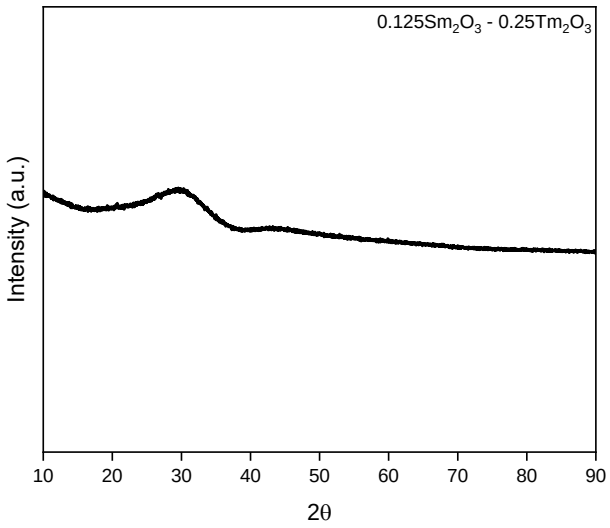


Figure 4.10 XRD pattern of $0.125Sm_2O_3 – 0.25Tm_2O_3$ sample

Simultaneous thermal analysis (STA) was used to evaluate the thermal properties of the synthesized $0.125Sm_2O_3$ - $0.25Tm_2O_3$ sample, and the resulting thermogram is shown in Figure 4.11. The sample of $0.125Sm_2O_3$ - $0.25Tm_2O_3$ has a detected glass transition onset (T_g) of 564 °C.

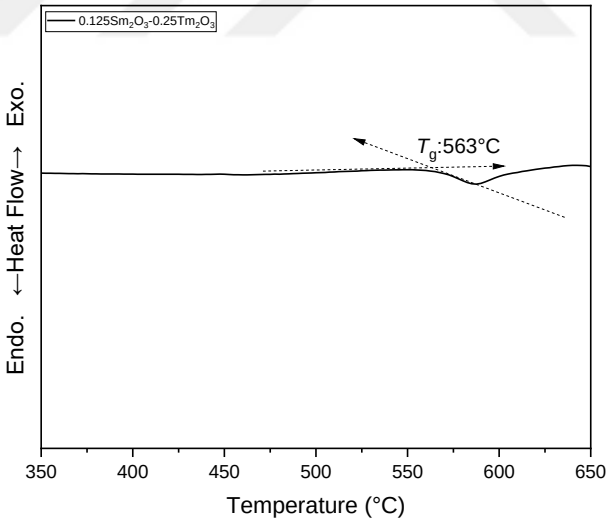


Figure 4.11 STA analysis of $0.125Sm_2O_3 – 0.25Tm_2O_3$ sample

The optical absorption spectrum of a sample made up of $0.125Sm_2O_3$ and $0.25Tm_2O_3$ is shown in Fig. 4.12 in the 190-1100 nm range. The optical absorption spectra show nine unique absorption peaks, six of which are related with the transitions of Sm^{3+}'s $^6H_{5/2}$ to $^4D_{3/2}$, $^6H_{5/2}$ to $^6P_{7/2}$, $^4L_{13/2}$, $^4I_{11/2}$, $^6H_{5/2}$ to $^6F_{11/2}$, and $^6H_{5/2}$ to $^6F_{9/2}$, respectively, and are situated at 360, 374, 402, 473, 941, and 1072 nm. The transitions of Tm^{3+} from $^3H_6$ to

$^1G_4$, $^3H_6$ to $^3F_3$, and $^3H_6$ to $^3H_4$ are represented by three additional peaks at wavelengths of 463, 683, and 790 nm, respectively.

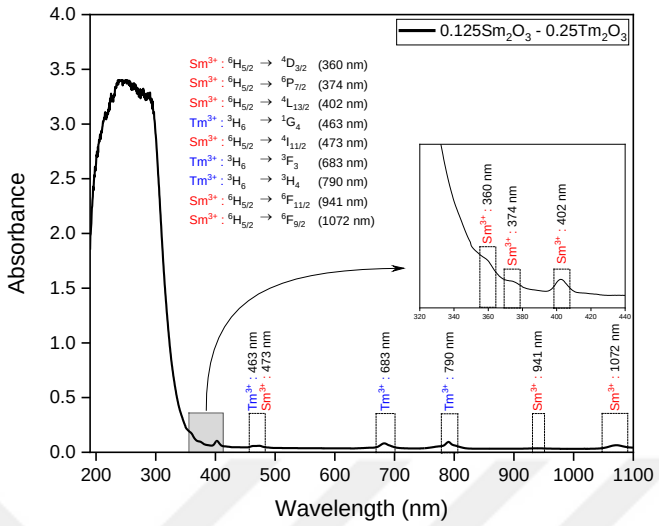


Figure 4.12 Optical absorption spectrum of $0.125Sm_2O_3 – 0.25Tm_2O_3$ sample

Figure 4.13 displays the excitation spectra for the sample made up of $0.125Sm_2O_3$ and $0.125Tm_2O_3$. They were determined by measuring the emission wavelengths in the 320-420 nm excitation range at 454, 565, 602, 648, and 707 nm, respectively.

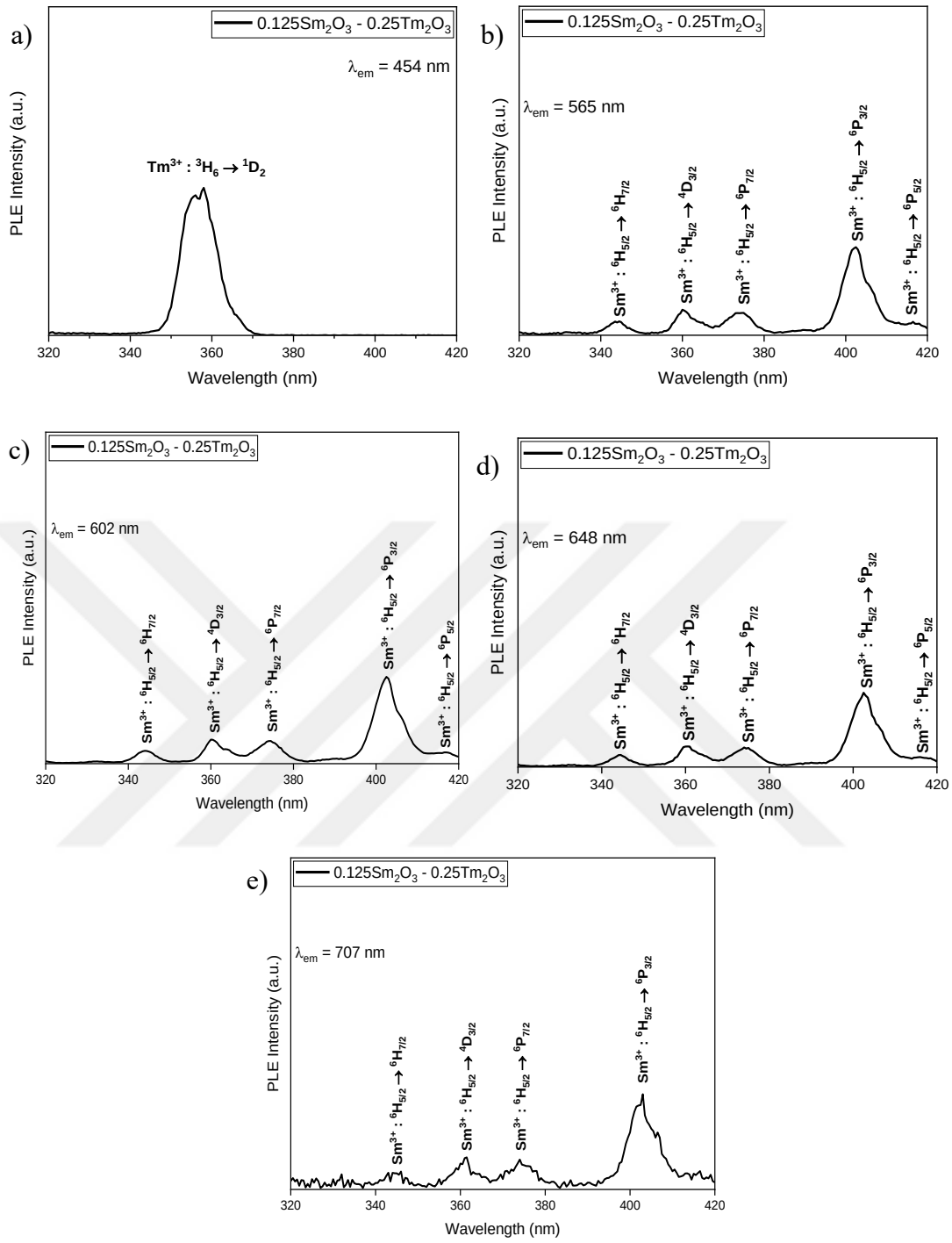


Figure 4.13 PL excitation spectra for different emission wavelengths of $0.125Sm_2O_3$ – $0.25Tm_2O_3$ sample

Figure 4.14 displays the PL spectra for the sample of $0.125Sm_2O_3$ and $0.25Tm_2O_3$. Under 360 nm excitation, six distinct peaks connected to Sm^{3+} and Tm^{3+} ions may be detected. Sm^{3+} ions emit four spectral lines at 565, 602, 648, and 707 nm as a result of the transitions $^4G_{5/2}$ to ^6H_J (J = 5/2, 7/2, 9/2, and 11/2), respectively, in contrast to Tm^{3+} ions,

which emit light at 454 and 482 nm as a result of the transitions $^1D_2$ to $^3F_4$ and $^1G_4$ to $^3H_6$, respectively.

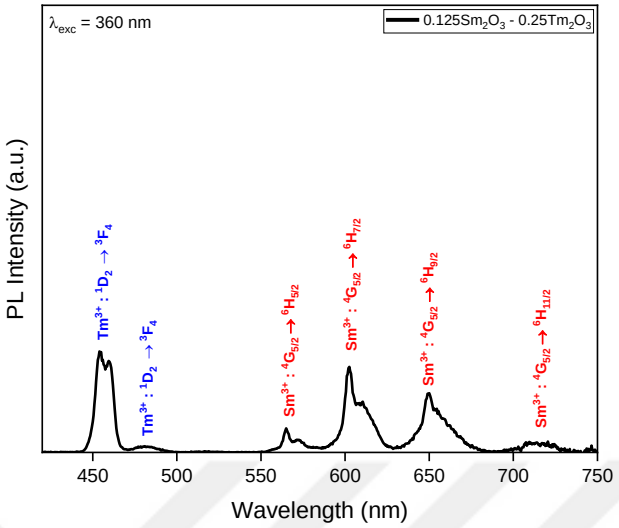


Figure 4.14 PL emission spectra of $0.125Sm_2O_3 – 0.25Tm_2O_3$ sample under 360 nm excitation

Figure 4.15 shows the macro image of a totally transparent $0.125Sm_2O_3$- $0.25Tm_2O_3$ sample excited at 360 nm. Through excitation at 360 nm, the red emission of Sm_2O_3 ions can be observed clearly with the human eye.

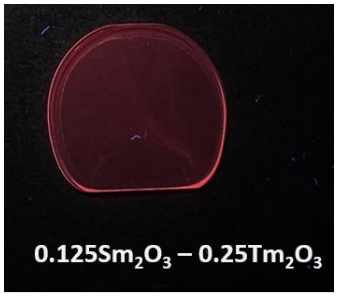


Figure 4.15 Macro photo of $0.125Sm_2O_3 – 0.25Tm_2O_3$ sample under 360 nm excitation

The CIE color coordinates for the $0.125Sm_2O_3$ - $0.25Tm_2O_3$ sample are shown in Figure 4.16. The color coordinates (0.4781, 0.2730) and CRI rating of 33 were discovered using the OSRAM color calculator application.

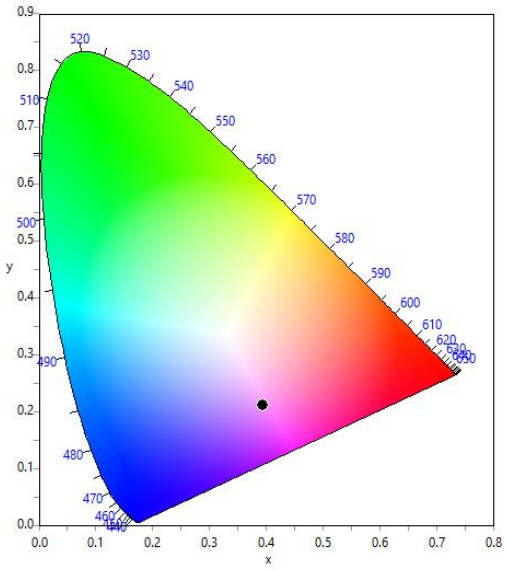


Figure 4.16 CIE color coordinates of $0.125Sm_2O_3 – 0.25Tm_2O_3$ sample under 360 nm excitation

4.1.3 $0.25Sm_2O_3 – 0.125Tm_2O_3$ Glass Sample

By using the conventional melt-quenching method, a glass sample made of $0.25Sm_2O_3$ and $0.125Tm_2O_3$ is created. This sample's glass composition is 15% Na_2O, 20% CaO, 5% Al_2O_3, 15% B_2O_3, 45% SiO_2, 0.125 Sm_2O_3 and 0.125 Tm_2O_3. Figure 4.17 depicts the macro image of a sample of the entirely transparent materials $0.125Sm_2O_3$ - $0.125Tm_2O_3$ sample.



Figure 4.17 Macro picture of $0.25Sm_2O_3 – 0.125Tm_2O_3$ sample

The manufactured $0.25Sm_2O_3$ - $0.125Tm_2O_3$ sample's amorphous nature is confirmed by the XRD pattern in Figure 4.18, which shows no discernible crystallization peaks.

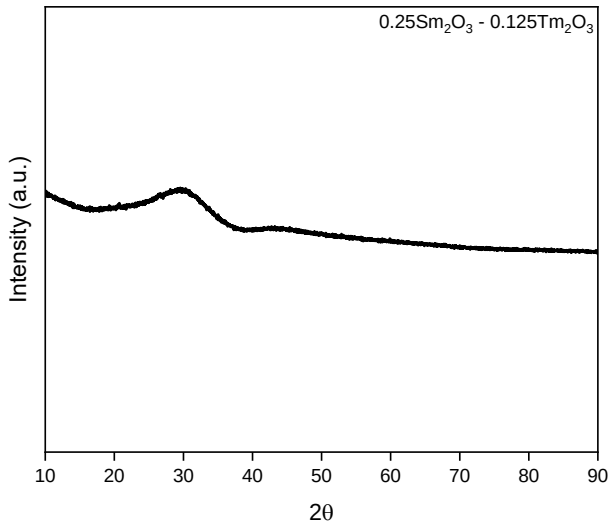


Figure 4.18 XRD pattern of $0.25Sm_2O_3 – 0.125Tm_2O_3$ sample

Simultaneous thermal analysis (STA) was used to examine the thermal characteristics of the synthesized $0.25Sm_2O_3$ - $0.125Tm_2O_3$ sample, and the resulting thermogram is shown in Figure 4.19. The sample of $0.25Sm_2O_3$ and $0.125Tm_2O_3$ has a glass transition onset (T_g) that is recognized at 564 °C.

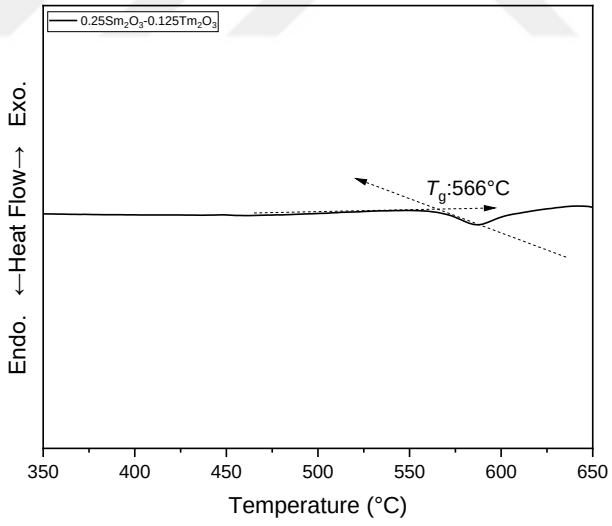


Figure 4.19 STA analysis of $0.25Sm_2O_3 – 0.125Tm_2O_3$ sample

The optical absorption spectrum of a sample constructed up of $0.25Sm_2O_3 – 0.125Tm_2O_3$ is shown in Fig.4.20 in the 190-1100 nm range. The optical absorption spectra show nine unique absorption peaks, six of which are related with the transitions of Sm^{3+}'s $^6H_{5/2}$ to $^4D_{3/2}$, $^6H_{5/2}$ to $^6P_{7/2}$, $^4L_{13/2}$, $^4I_{11/2}$, $^6H_{5/2}$ to $^6F_{11/2}$, and $^6H_{5/2}$ to $^6F_{9/2}$, respectively, and are situated at 360, 374, 402, 473, 941, and 1072 nm. The transitions of Tm^{3+} from $^3H_6$ to

$^1G_4$, $^3H_6$ to $^3F_3$, and $^3H_6$ to $^3H_4$ are represented by three additional peaks at wavelengths of 463, 683, and 790 nm, respectively.

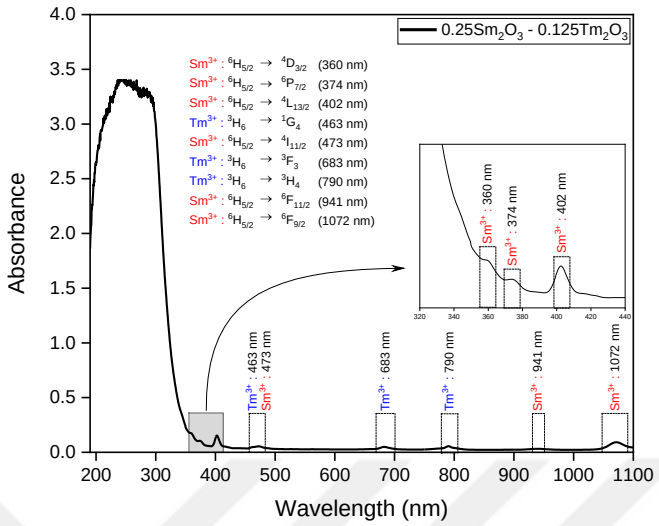


Figure 4.20 Optical absorption spectrum of $0.25Sm_2O_3 – 0.125Tm_2O_3$ sample

Figure 4.21 displays the excitation spectra for the sample made up of $0.25Sm_2O_3$ and $0.125Tm_2O_3$. They were determined by measuring the emission wavelengths in the 320-420 nm excitation range at 454, 565, 602, 648, and 707 nm, respectively.

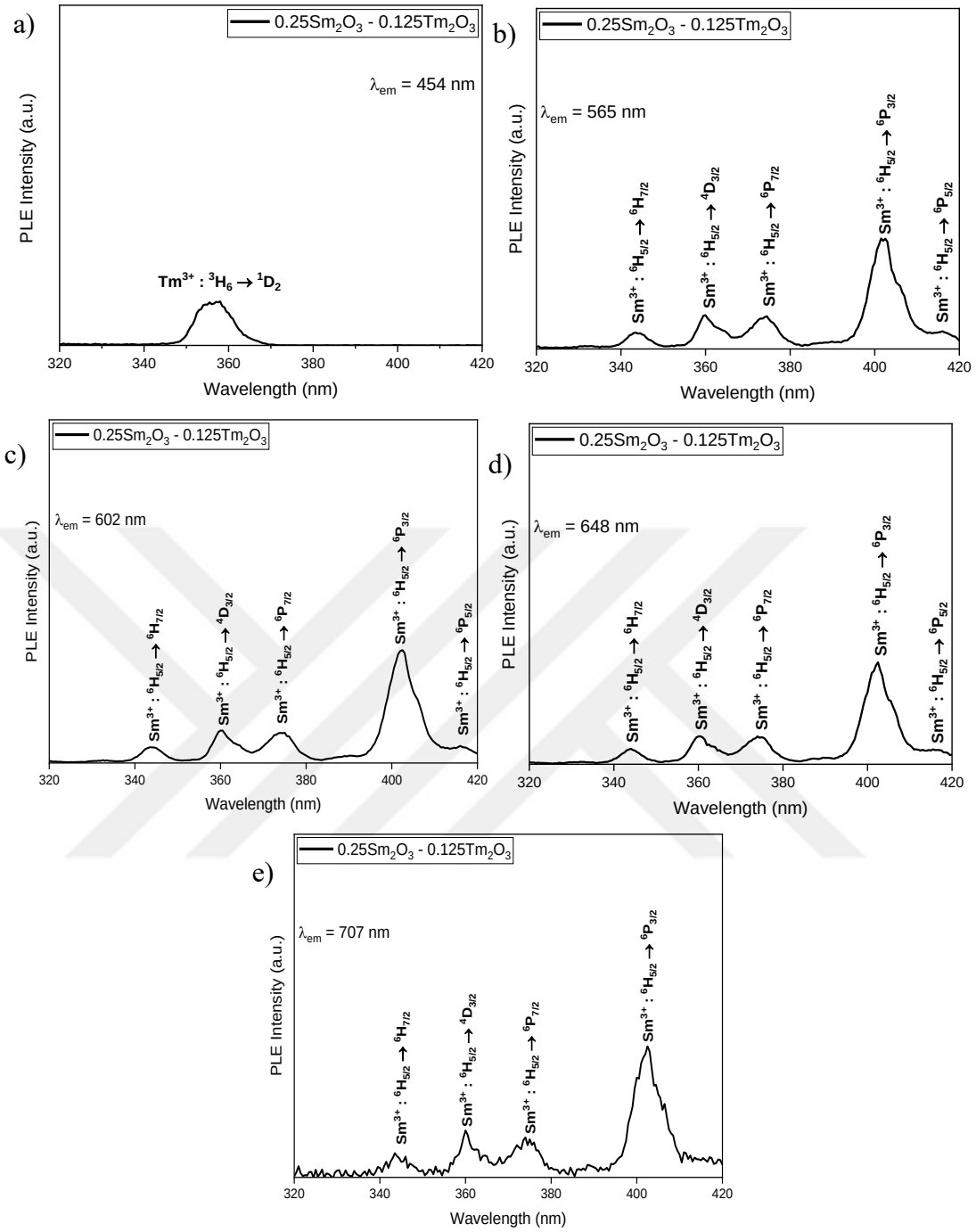


Figure 4.21 PL excitation spectra for different emission wavelengths of $0.25Sm_2O_3$ – $0.125Tm_2O_3$ sample

Figure 4.22 displays the PL spectra for the sample of $0.125Sm_2O_3$ and $0.25Tm_2O_3$. Under 360 nm excitation, six distinct peaks connected to Sm^{3+} and Tm^{3+} ions may be detected. Sm^{3+} ions emit four spectral lines at 565, 602, 648, and 707 nm as a result of the transitions $^4G_{5/2}$ to ^6H_J (J = 5/2, 7/2, 9/2, and 11/2), respectively, in contrast to Tm^{3+} ions,

which emit light at 454 and 482 nm as a result of the transitions $^1D_2$ to $^3F_4$ and $^1G_4$ to $^3H_6$, respectively.

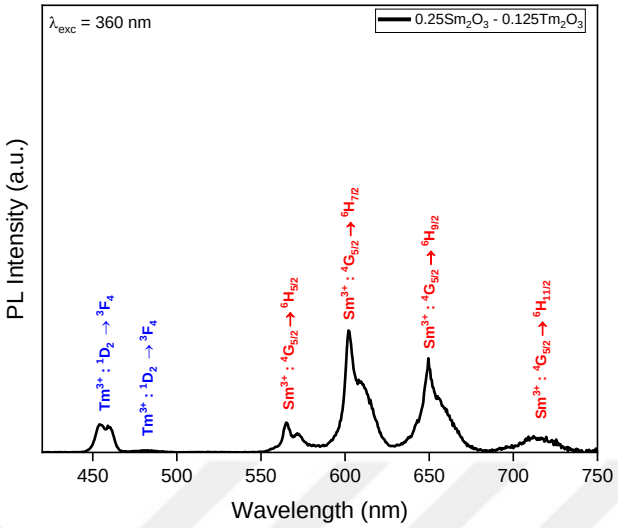


Figure 4.22 PL emission spectra of $0.25Sm_2O_3 – 0.125Tm_2O_3$ sample under 360 nm excitation

Figure 4.23 shows the macro image of a transparent $0.25Sm_2O_3$- $0.125Tm_2O_3$ sample excited at 360 nm. Through stimulation at 360 nm, red Sm_2O_3 ions emission is plainly visible to the unaided eye.

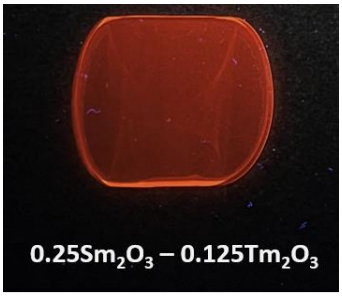


Figure 4.23 Macro photo of $0.25Sm_2O_3 – 0.125Tm_2O_3$ sample under 360 nm excitation

Figure 4.24 shows the CIE color coordinates for the $0.25Sm_2O_3 – 0.125Tm_2O_3$ sample. The color values (0.4781, 0.2730) and 33 CRI were calculated using the OSRAM color calculator tool.

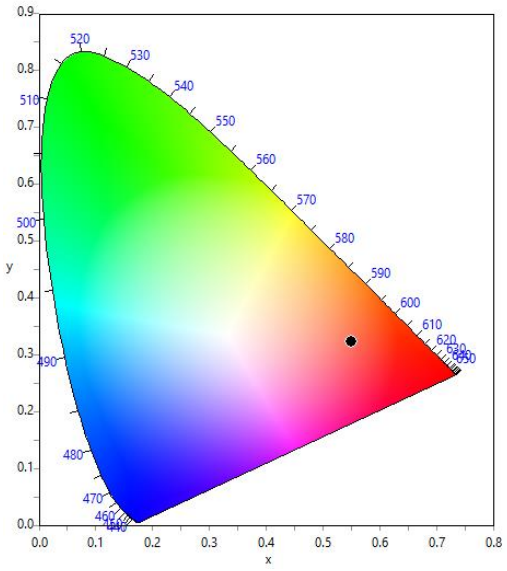


Figure 4.24 CIE color coordinates of $0.25Sm_2O_3 – 0.125Tm_2O_3$ sample under 360 nm excitation

4.1.4 $0.25Sm_2O_3 – 0.25Tm_2O_3$ Glass Sample

The traditional melt-quenching method is used to create a glass sample that is $0.25Sm_2O_3 – 0.25Tm_2O_3$. The glass in this sample is composed 15% Na_2O, 20% CaO, %5 Al_2O_3, %15 B_2O_3, %45 SiO_2, %0.125Sm_2O_3 and %0.25Tm_2O_3. Figure 4.25 displays a macro image of a fully transparent $0.25Sm_2O_3 – 0.25Tm_2O_3$ sample.



Figure 4.25 Macro picture of $0.25Sm_2O_3 – 0.25Tm_2O_3$ sample

The XRD pattern in Figure 4.26, which shows no apparent crystallization peaks, confirms the amorphous nature of the synthesized $0.25Sm_2O_3 – 0.25Tm_2O_3$ sample.

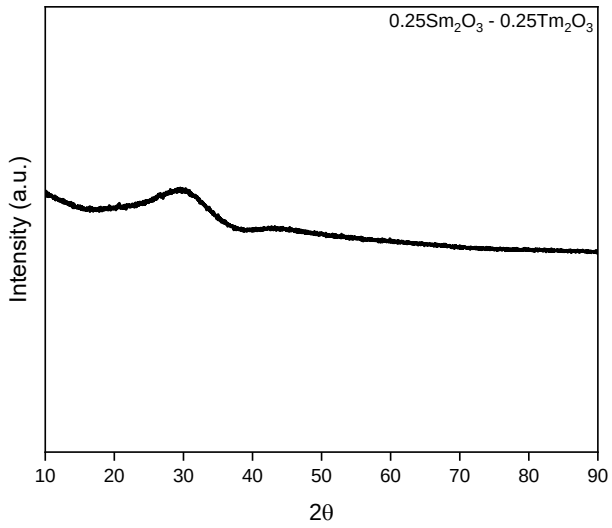


Figure 4.26 XRD pattern of $0.25Sm_2O_3 – 0.25Tm_2O_3$ sample

In order to evaluate the thermal characteristics of the synthesized $0.25Sm_2O_3 – 0.25Tm_2O_3$ sample, simultaneous thermal analysis (STA) was used. The thermogram is shown in Figure 4.27. The sample of $0.25Sm_2O_3 – 0.25Tm_2O_3$ has a detected glass transition onset (T_g) of 564 °C.

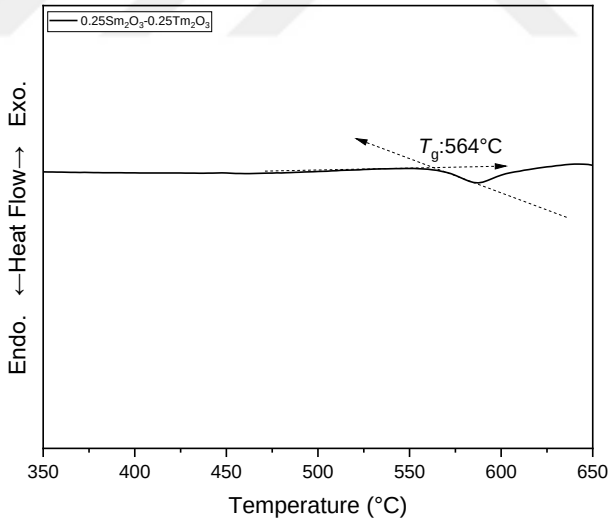


Figure 4.27 STA analysis of $0.25Sm_2O_3 – 0.25Tm_2O_3$ sample

The optical absorption spectrum of the $0.25Sm_2O_3 – 0.25Tm_2O_3$ sample between 190 and 1100 nm is shown in Fig. 4.28. The optical absorption spectra exhibit nine different absorption peaks, six of which are positioned at 360, 374, 402, 473, 941, and 1072 nm and are connected to the transitions of Sm^{3+}'s $^6H_{5/2}$ to $^4D_{3/2}$, $^6H_{5/2}$ to $^6P_{7/2}$, $^4L_{13/2}$, $^4I_{11/2}$, $^6H_{5/2}$ to $^6F_{11/2}$, and $^6H_{5/2}$ to $^6F_{9/2}$, respectively. Additionally, three peaks are observed at

wavelengths of 463, 683, and 790 nm, respectively, which represent the transitions of Tm^{3+} from $^3H_6$ to $^1G_4$, $^3H_6$ to $^3F_3$, and $^3H_6$ to $^3H_4$.

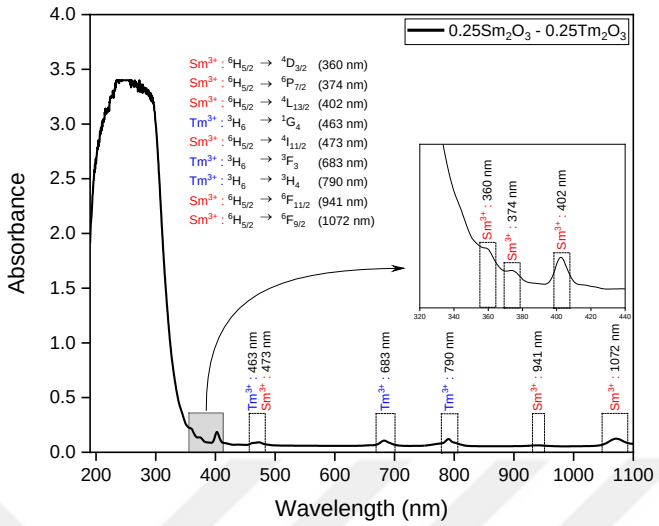


Figure 4.28 Optical absorption spectrum of $0.25Sm_2O_3 – 0.25Tm_2O_3$ sample

Figure 4.29 displays the excitation spectra for the sample made up of $0.125Sm_2O_3$ and $0.125Tm_2O_3$. They were determined by measuring the emission wavelengths in the 320-420 nm excitation range at 454, 565, 602, 648, and 707 nm, respectively.

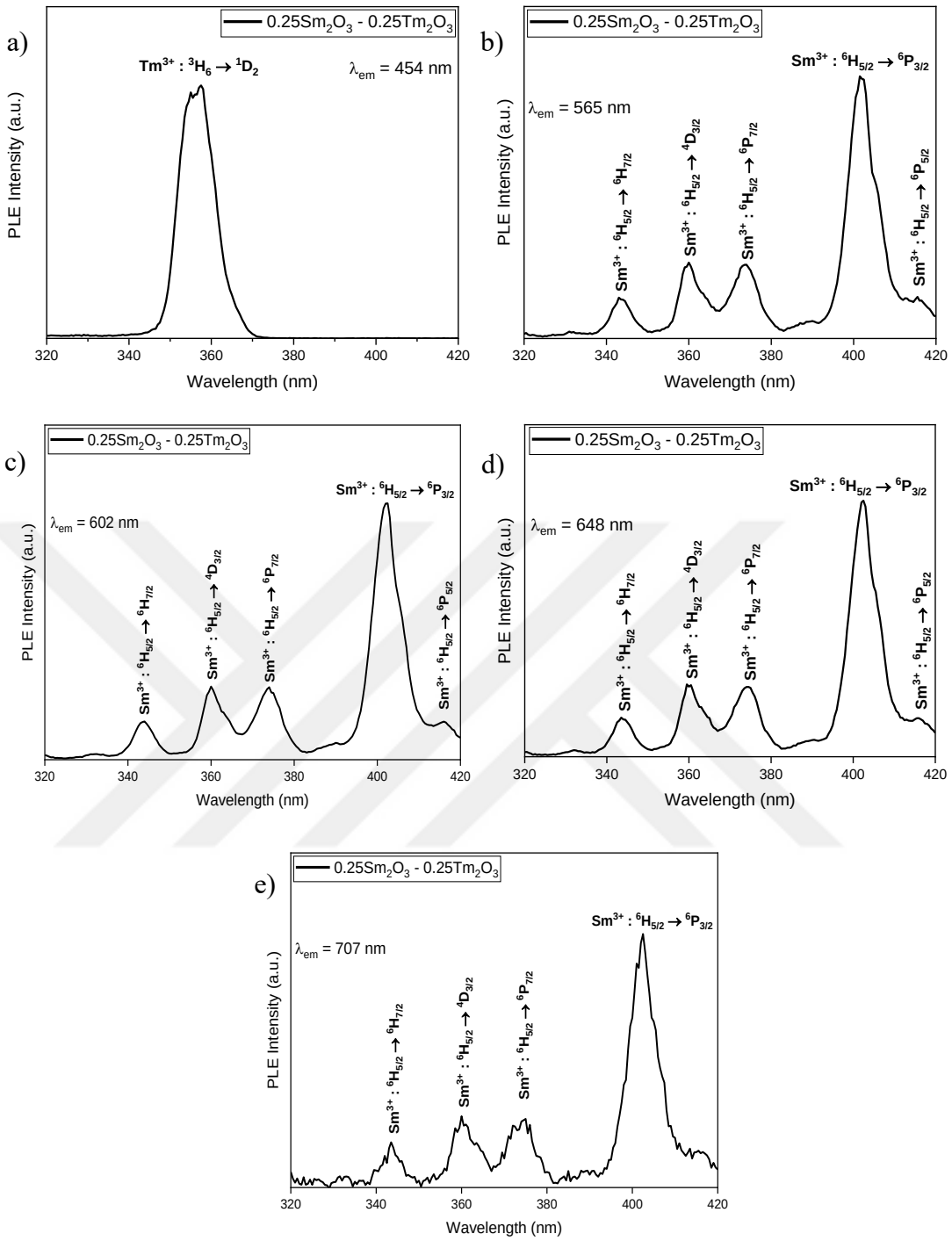


Figure 4.29 PL excitation spectra for different emission wavelengths of $0.25Sm_2O_3$ – $0.25Tm_2O_3$ sample

In Fig. 4.30, the PL spectra for the sample of $0.25Sm_2O_3$ – $0.25Tm_2O_3$ are presented. Under 360 nm excitation, six distinct peaks associated with the Sm^{3+} and Tm3+ ions are visible. As a result of the transitions $^1D_2$ to $^3F_4$ and $^1G_4$ to $^3H_6$, respectively, Sm^{3+} and Tm^{3+} ions produce light at 454 and 482 nm, whereas Sm^{3+} ions emit four spectral lines at

565, 602, 648, and 707 nm as a result of the transitions $^4G_{5/2}$ to ^6H_J (J = 5/2, 7/2, 9/2, and 11/2), respectively.

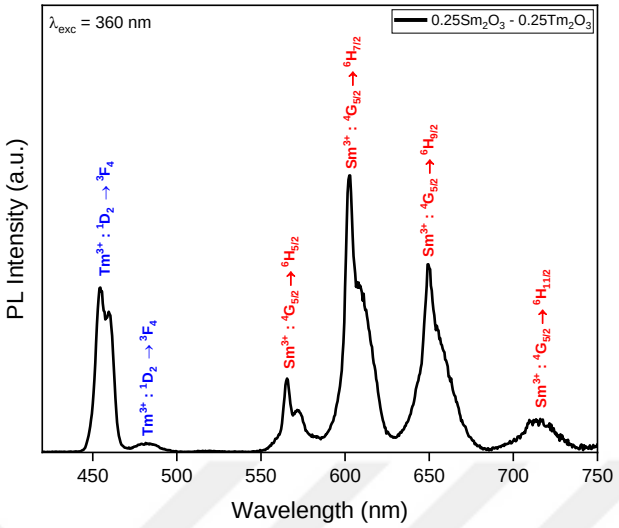


Figure 4.30 PL emission spectra of $0.25Sm_2O_3 – 0.25Tm_2O_3$ sample under 360 nm excitation

In Figure 4.31, a 360 nm excitation is used to create a macro image of a totally transparent $0.25Sm_2O_3 – 0.25Tm_2O_3$ sample. With 360 nm excitation, red emission of Sm_2O_3 ions is readily visible to the human eye.

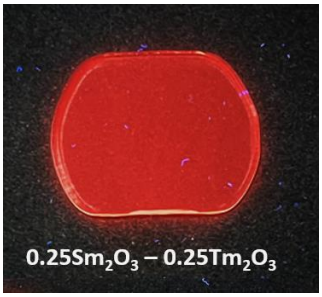


Figure 4.31 Macro photo of $0.25Sm_2O_3 – 0.25Tm_2O_3$ sample under 360 nm excitation

The CIE color coordinates are shown in Figure 4.32 for the $0.25Sm_2O_3 – 0.25Tm_2O_3$ sample. The color coordinates were (0.4781, 0.2730) and the CRI value was 33, both of which were obtained using the OSRAM color calculator program.

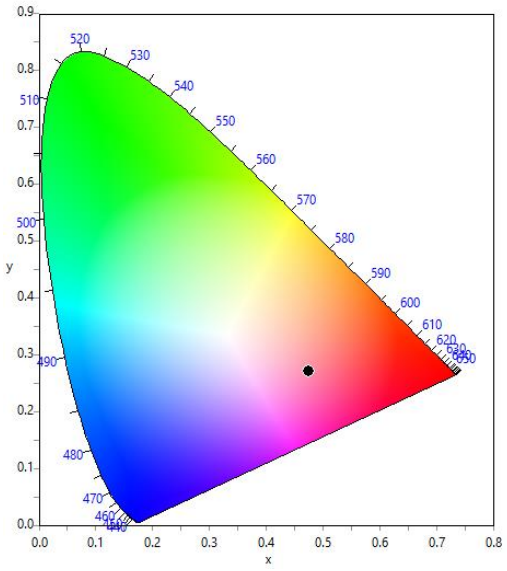


Figure 4.32 CIE color coordinates of $0.25Sm_2O_3 – 0.25Tm_2O_3$ sample under 360 nm excitation

4.1.5 $0.50Sm_2O_3 – 0.50Tm_2O_3$ Glass Sample

A glass sample made of $0.50Sm_2O_3 – 0.50Tm_2O_3$ was created using the traditional melt-quenching method. This sample's glass has the following compositions: 15% Na_2O, 20% CaO, %5 Al_2O_3, %15 B_2O_3, %45 SiO_2, %0.125Sm_2O_3 and %0.25Tm_2O_3. Figure 4.33 depicts the macro photo of the completely transparent $0.50Sm_2O_3 – 0.50Tm_2O_3$ sample.

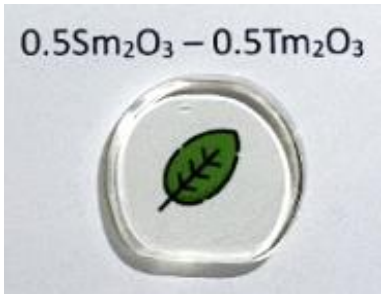


Figure 4.33 Macro picture of $0.50Sm_2O_3 – 0.50Tm_2O_3$ sample

The synthetic $0.50Sm_2O_3 – 0.50Tm_2O_3$ sample's amorphous nature is supported by the XRD pattern in Figure 4.34, which shows not any apparent crystallization peaks.

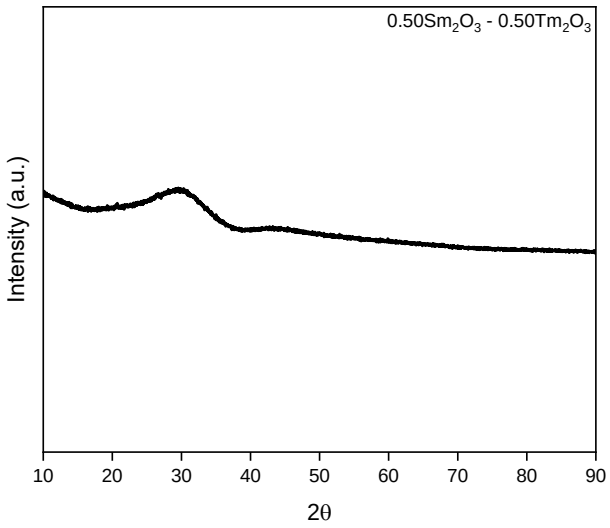


Figure 4.34 XRD pattern of $0.50Sm_2O_3 – 0.50Tm_2O_3$ sample

Through simultaneous thermal analysis (STA), the thermal characteristics of the synthesized $0.50Sm_2O_3 – 0.50Tm_2O_3$ sample were examined. The thermogram is shown in Figure 4.35. Detected at 564 °C is the glass transition onset (T_g) of the $0.50Sm_2O_3 – 0.50Tm_2O_3$ sample.

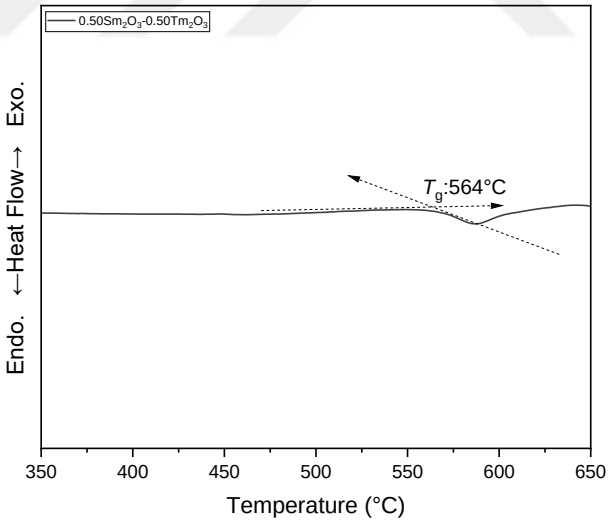


Figure 4.35 STA analysis of $0.50Sm_2O_3 – 0.50Tm_2O_3$ sample

The optical absorption spectrum of the $0.50Sm_2O_3 – 0.50Tm_2O_3$ sample is shown in Fig.4.36 in the 190-1100 nm range. The optical absorption spectra show nine different absorption peaks, six of which are related to the transitions of Sm^{3+}'s $^6H_{5/2}$ to $^4D_{3/2}$, $^6H_{5/2}$ to $^6P_{7/2}$, $^4L_{13/2}$, $^4I_{11/2}$, $^6H_{5/2}$ to $^6F_{11/2}$, and $^6H_{5/2}$ to $^6F_{9/2}$, respectively. These transitions are centered at 360, 374, 402, 473, 941, and 1072 nm, respectively. In addition, three peaks

are observed at wavelengths of 463, 683, and 790 nm, which, respectively, represent the transitions of Tm^{3+} from $^3H_6$ to $^1G_4$, $^3H_6$ to $^3F_3$, and $^3H_6$ to $^3H_4$, are related to these transitions.

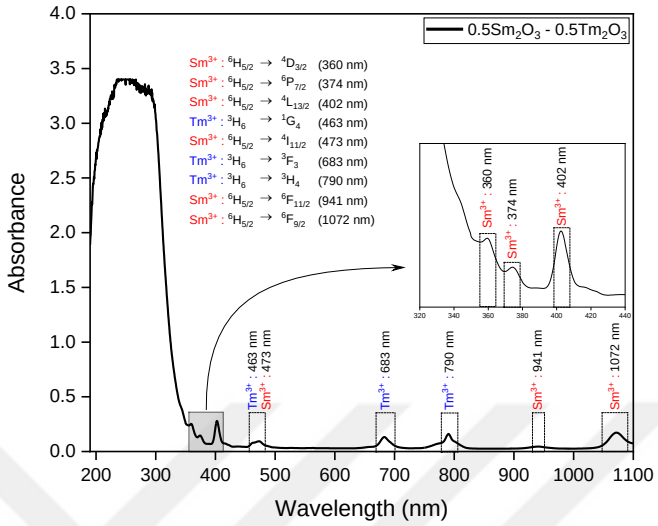


Figure 4.36 Optical absorption spectrum of $0.50Sm_2O_3 – 0.50Tm_2O_3$ sample

In Fig. 4.37, the excitation spectra of the $0.50Sm_2O_3 – 0.50Tm_2O_3$ sample are displayed. They were discovered by measuring the emission wavelengths at, successively, 454, 565, 602, 648, and 707 nm in the 320-420 nm excitation range.

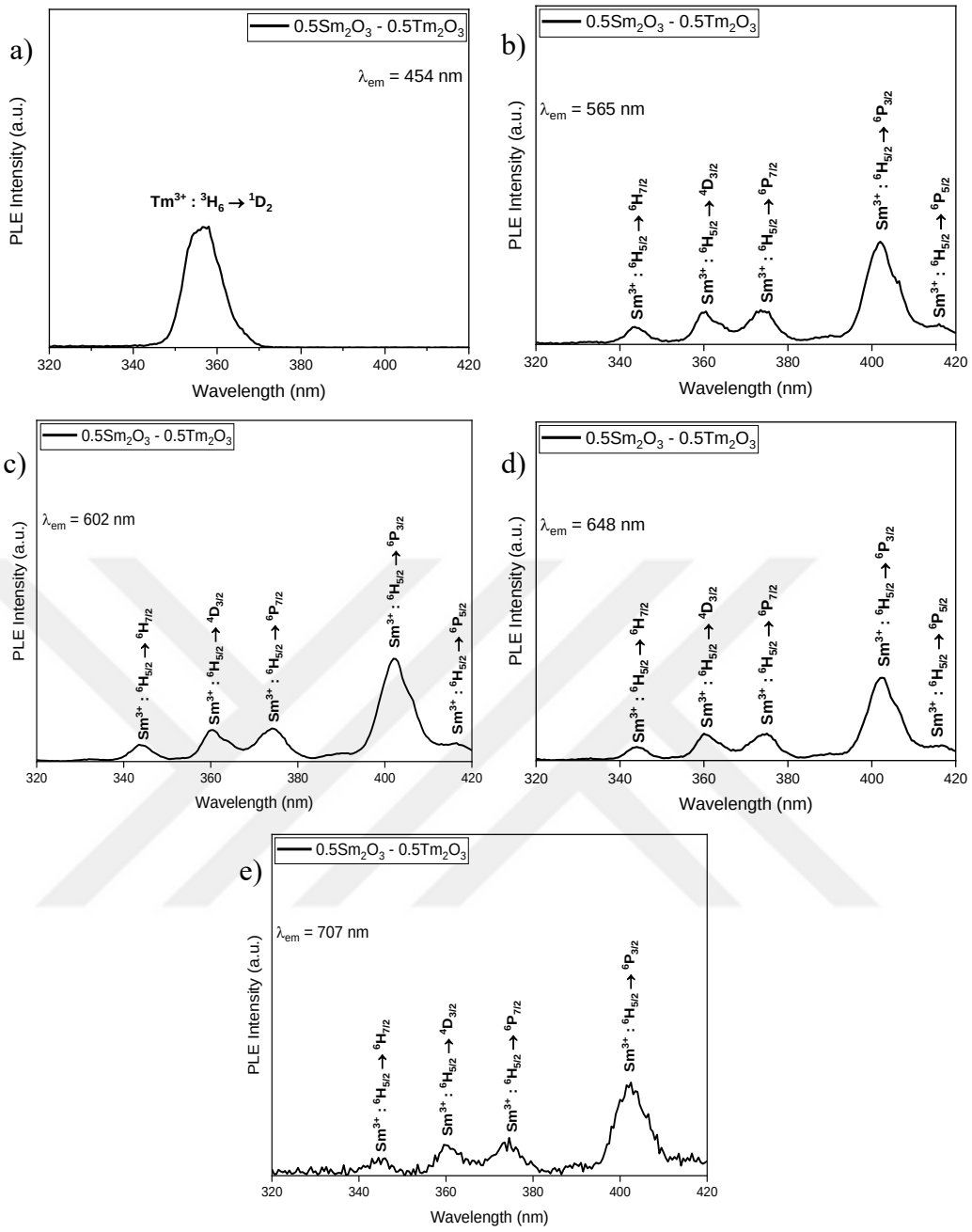


Figure 4.37 PL excitation spectra for different emission wavelengths of $0.50Sm_2O_3 – 0.50Tm_2O_3$ sample

Figure 4.38 depicts the PL spectra for the sample of $0.50Sm_2O_3 – 0.50Tm_2O_3$. Under 360 nm excitation, six distinct peaks associated with Sm^{3+} and Tm^{3+} ions can be observed.Sm^{3+} and Tm^{3+} ions emit light at 454 and 482 nm as a consequence of the transitions $^1D_2$ to $^3F_4$ and $^1G_4$ to $^3H_6$, respectively, whereas Sm^{3+} ions emit four spectral lines at 565, 602, 648, and 707 nm as a result of the transitions $^4G_{5/2}$ to ^6H_J (J = 5/2, 7/2, 9/2, and 11/2), respectively.

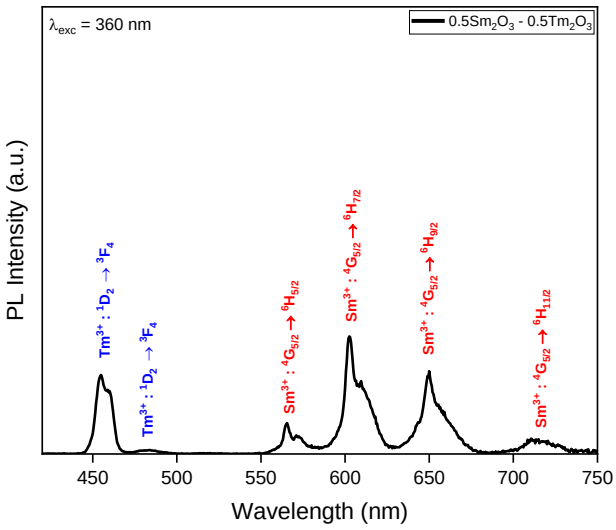


Figure 4.38 PL emission spectra of $0.50Sm_2O_3 – 0.50Tm_2O_3$ sample under 360 nm excitation

Figure 4.39 displays the macro image of a totally transparent $0.50Sm_2O_3 – 0.50Tm_2O_3$ sample excited at 360 nm. With 360 nm excitation, red emission of Sm_2O_3 ions is readily visible to the human eye.

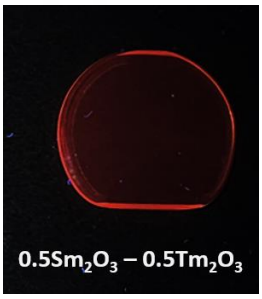


Figure 4.39 Macro photo of $0.50Sm_2O_3 – 0.50Tm_2O_3$ sample under 360 nm excitation

The CIE color coordinates for the sample $0.50Sm_2O_3 – 0.50Tm_2O_3$ are shown in Figure 4.40. The color coordinates (0.4781, 0.2730) and CRI value of 33 were found using the OSRAM color calculator application.

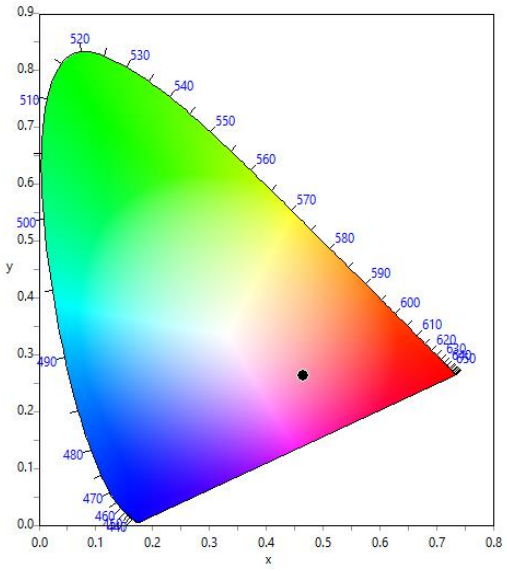


Figure 4.40 CIE color coordinates of $0.50Sm_2O_3 – 0.50Tm_2O_3$ sample under 360 nm excitation

4.2 Discussion

All the samples were compiled into graphics corresponding to their optical, thermal, photoluminescence, color, and lifetime properties in order to discuss the experimental findings. Then, $0.25Sm_2O_3$-$0.25Tm_2O_3$ sample was selected as the most suitable sample for creating a plant growth LED device. After that, the newly produced plant growth LED was subjected to a number of tests such as operational stability and photoluminescence properties. Subsequently, for comparison two plant growth LED systems were constructed, experimental group contains this developed plant growth LED and two commercial white LEDs, and the control group contains commercial plant growth LED along with a white LED. Following that, Romaine lettuces were planted in a specific plant growth cabinet utilizing these two LED systems, and the outcomes have been discussed.

4.2.1 Thermal and Structural Analysis

The XRD graphs in Figure 4.41a proved that the produced luminescent glass samples are amorphous. The figure shows that there are no crystalline peaks other than a broad hump between 25° and 35°, indicating that amorphous samples were produced.

In order to properly define the annealing conditions, the thermal characteristics of the glass samples are examined using simultaneous thermal analysis (STA).

The STA curves of all synthesized materials are shown in Figure 4.41b, and the glass transition onsets for each sample were determined to be 566°C, 564°C, 565°C, 564°C, and 563°C, respectively. Based on these findings, 470 °C is chosen as the annealing temperature, which is lower than the glass transition temperature (T_g) to avoid crystallization, and the annealing process is carried out for 5 hours. The STA findings show that the glass samples can tolerate high temperatures and heating-cooling cycles without losing their structural integrity, which is a crucial need for LED applications.

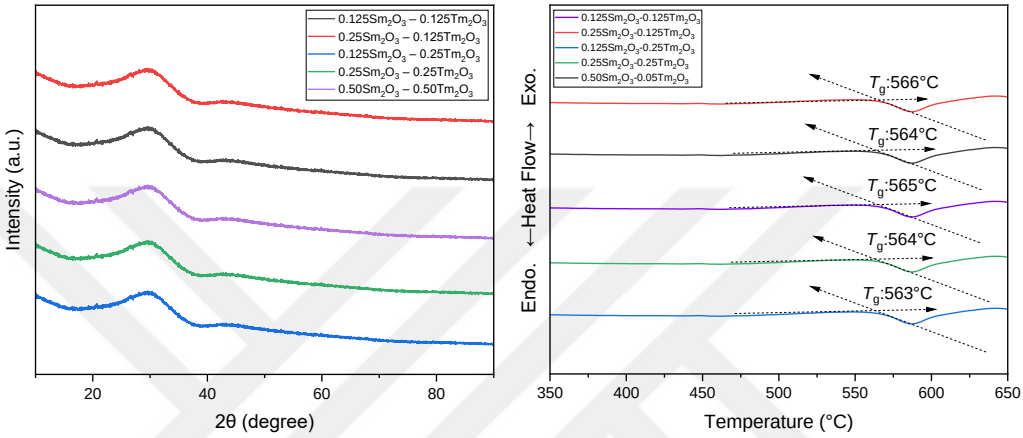


Figure 4.41 a) XRD patterns, and b) STA thermograms, showing amorphous nature and thermal behavior of produced glass samples, respectively.

4.2.2 Optical and Photoluminescence Analysis

In Figure 4.42, nine distinct absorption peaks can be seen in the optical absorption spectra, six of which are located at 360, 374, 402, 473, 941, and 1072 nm and are associated with the transitions of Sm^{3+}'s $^6H_{5/2}$ to $^4D_{3/2}$, $^6H_{5/2}$ to $^6P_{7/2}$, $^4L_{13/2}$, $^4I_{11/2}$, $^6H_{5/2}$ to $^6F_{11/2}$, and $^6H_{5/2}$ to $^6F_{9/2}$, respectively [88]. The transitions of Tm^{3+} from $^3H_6$ to $^1G_4$, $^3H_6$ to $^3F_3$, and $^3H_6$ to $^3H_4$ are also visible as three peaks at 463, 683, and 790 nm, respectively [89]. The $0.5Sm_2O_3$ - $0.5Tm_2O_3$ sample exhibits the highest absorbance of all the samples. Generally, the absorbance increases with increasing mol% of lanthanide ions.

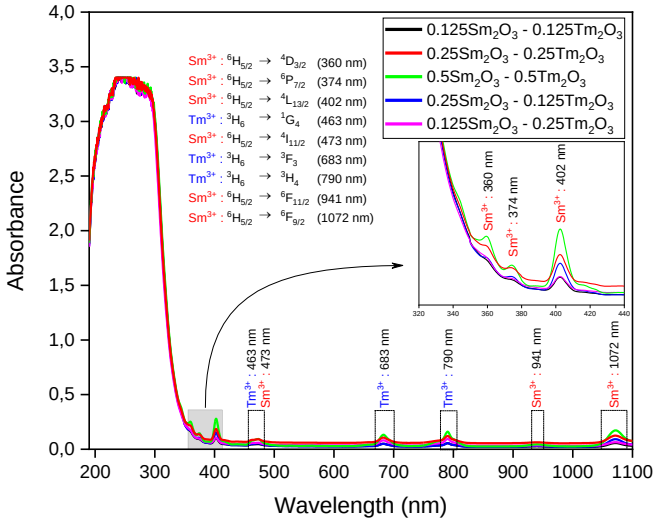


Figure 4.42 Optical absorption spectra of Sm^{3+} and Tm^{3+} co-doped glass samples

The excitation spectra of Tm^{3+} ions and Sm^{3+} ions in co-doped Sm^{3+} and Tm^{3+} glass samples are shown in Figure 4.43. These spectra were obtained by measuring the emission wavelengths at 454 nm and 648 nm, respectively, in the excitation wavelength range of 320-420 nm. These specific emissions were chosen because they most closely correspond to the absorption zones of the chlorophyll a and chlorophyll b pigments that are used in photosynthesis. As a result, the transition from the ground state ($^3H_6$) to the excited state $^1D_2$ is responsible for the single peak seen for Tm^{3+} (see Figure 4.43a). The transitions from the ground state ($^6H_{5/2}$) to the excited states ($^6H_{7/2}$, $^4D_{3/2}$, $^6P_{7/2}$, $^6P_{3/2}$, and $^6P_{5/2}$) are attributed to the excitation peaks seen for Sm^{3+} under 648 nm emission wavelength. Among all transitions that have been observed, the $^6H_{5/2}$ to $^6P_{3/2}$ transition has the highest intensity (Figure 4.43b).

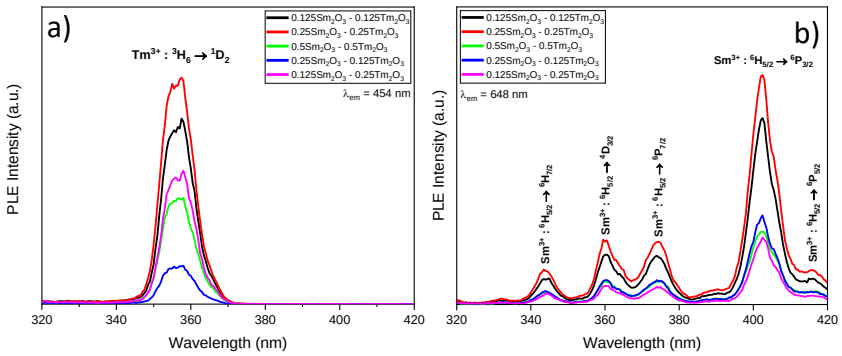


Figure 4.43 Excitation spectra of Sm^{3+} and Tm^{3+} co-doped glasses, with a) monitoring of 454 nm Tm^{3+} ion emission, b) monitoring of 648 nm Sm^{3+} ion emission

As seen in Figure 4.44, the results of PL excitation experiments show that the Sm^{3+} and Tm^{3+} ions have a mutual excitation area approximately at 360 nm. Therefore, for all PL measurements, 360 nm is chosen as the common excitation wavelength of Sm^{3+} and Tm^{3+} ions.

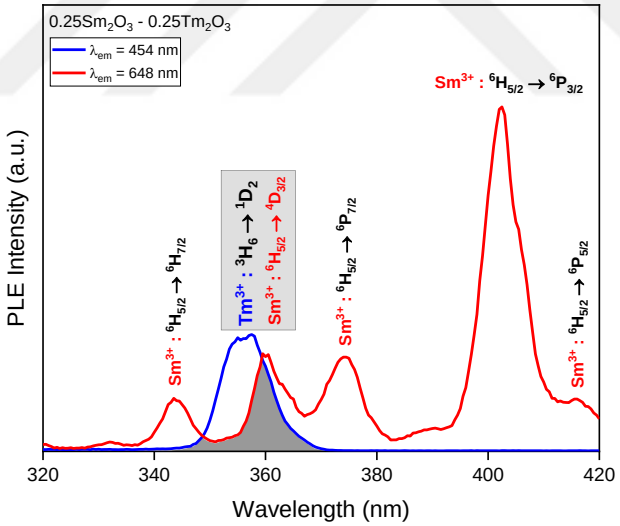


Figure 4.44 Intersection area for PL excitation of Sm^{3+} and Tm^{3+} ions for selected $0.25Sm_2O_3$ - $0.25Tm_2O_3$ sample

For Sm^{3+} and Tm^{3+} co-doped glasses, Figure 4.45 displays the PL spectra, and Figure 4.46 displays the matching CIE chromaticity diagram. Six separate peaks linked to Sm^{3+} and Tm^{3+} ions are seen under 360 nm excitation. Tm^{3+} and Sm^{3+} ions emit light at 454 and 482 nm, respectively, as a result of the transitions $^1D_2$ to $^3F_4$ and $^1G_4$ to $^3H_6$, whereas Sm^{3+} ions emit light at 565, 602, 648, and 707 nm, respectively, as a result of the transitions $^4G_{5/2}$ to ^6H_J (J = 5/2, 7/2, 9/2, and 11/2).

As a result of the strong $^4G_{5/2}$ to $^6H_{9/2}$ transition intensity of Sm^{3+}, the $^3F_2$ to $^3H_6$ and $^3F_3$ to $^3H_6$ transitions of Tm^{3+} are not considered in Figure 4.46. When Sm^{3+} and Tm^{3+} dopant concentrations reach a saturation point, the intensity of PL emission bands increases until that point, at which point it drops as a result of PL quenching. The dopant concentration, however, has little impact on the location or shape of the bands [90, 91].

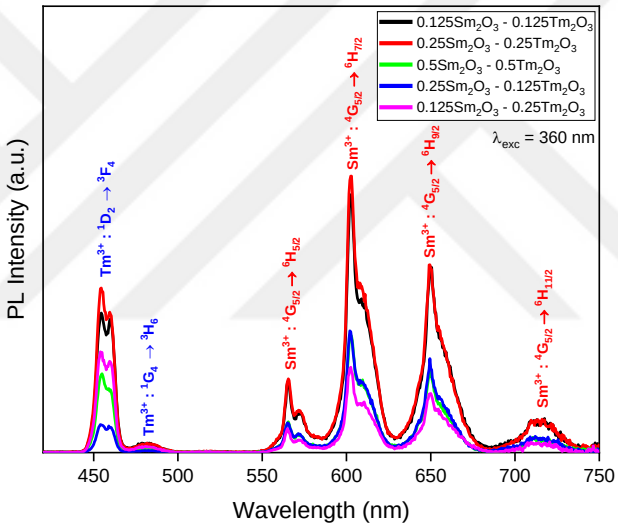


Figure 4.45 PL emission spectra of the Sm^{3+} and Tm^{3+} co-doped glasses under 360 nm excitation

The CIE color coordinates for the Sm^{3+} and Tm^{3+} co-doped glasses are shown in Figure 4.46. To find the ideal lanthanide ion concentrations to generate brilliant blue and red-light emissions, numerous experiments have been carried out. For instance, the luminous glass samples display red color coordinates on the CIE chromaticity diagram when the Tm_2O_3 and Sm_2O_3 doping concentrations are set to 0.125 and 0.25 mol%, respectively, because of the strong red emission of Sm^{3+}. On the other hand, when the Tm^{3+} ion concentration is high, as is the case when the Tm_2O_3 and Sm_2O_3 doping levels are set to 0.25 and 0.125 mol%, respectively, the emission lacks red color. So, based on the

maximum intensity, the optimal doping doses of 0.25 mol% Tm_2O_3 and 0.25 mol% Sm_2O_3 are identified and used in this work for blue- and red-light emission experiments.

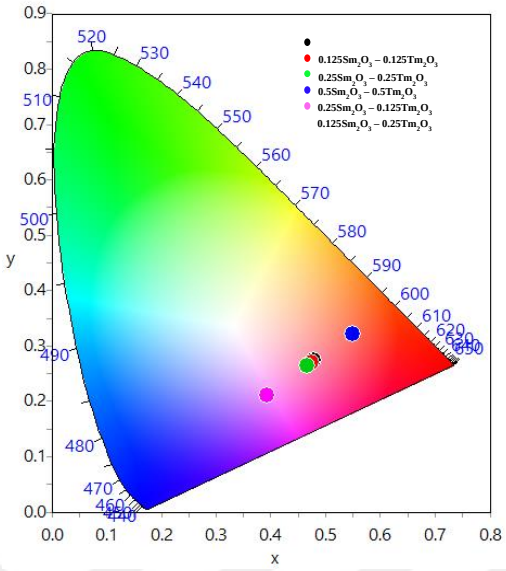


Figure 4.46 CIE color coordinates of Sm^{3+} and Tm^{3+} co-doped glasses under 360 nm excitation

In addition to that, relevant color coordinates of Sm^{3+} and Tm^{3+} co-doped glasses are listed in Table 4.1 as a written proof of CIE diagrams which displayed in Figure 4.47.

Table 4. 1 Color coordinates, PLQY and CRI values of Sm^{3+} and Tm^{3+} co-doped glasses under 360 nm excitation

Sample	Color Coordinates (x, y)	PLQY (%)	CRI
$0.125Sm_2O_3 – 0.125Tm_2O_3$	0.4781, 0.2730	23.57	33
$0.125Sm_2O_3 – 0.25Tm_2O_3$	0.3936, 0.2107	12.73	14
$0.25Sm_2O_3 – 0.125Tm_2O_3$	0.5494, 0.3220	31.41	41
$0.25Sm_2O_3 – 0.25Tm_2O_3$	0.4746, 0.2709	56.26	33
$0.50Sm_2O_3 – 0.50Tm_2O_3$	0.4664, 0.2639	15.19	30

Moreover, another reason for 0.25 mol% Tm_2O_3 and 0.25 mol% Sm_2O_3 sample was chosen is it demonstrates the highest PLQY among all other samples, with a value of 56.26% under 360 nm excitation. The PLQY and CRI values of other Sm^{3+} and Tm^{3+} co-doped glasses are listed in Table 4.1.

4.2.3 Lifetime Analysis and Energy Transfer Mechanisms

In order to investigate lifetime properties of selected 0.25Sm_2O_3-0.25 Tm_2O_3 sample, we need to separate the lanthanide components. So as to conduct lifetime analysis, a set of new glass samples was produced as reference. These samples are intended to search for the energy transitions between two lanthanide ions.

4.2.3.1 PL and Lifetime Analysis of Reference Sample 1 (0.25Tm_2O_3)

Reference Sample 1 contains the following composition: 15% Na_2O, 20% CaO, %5 Al_2O_3, %15 B_2O_3, %45 SiO_2, %0.25Tm_2O_3. The Figure 4.47a depicts the PL spectra for the sample of Sample 1. Under 360 nm excitation, four distinct peaks associated with Tm^{3+} ions can be seen. Tm^{3+} ions emit four spectral lines at 454, 480, 655 and 675 because of the transitions at $^1D_2$ to $^3F_4$, $^1G_4$ to $^3H_6$, $^3F_2$ to $^3H_6$ and $^3F_3$ to $^3H_6$, respectively. In the Figure 4.47b, lifetime analysis of Sample 1 is given and the $\chi 2$ and τ values are found 1.052 and 15.424 µs, respectively.

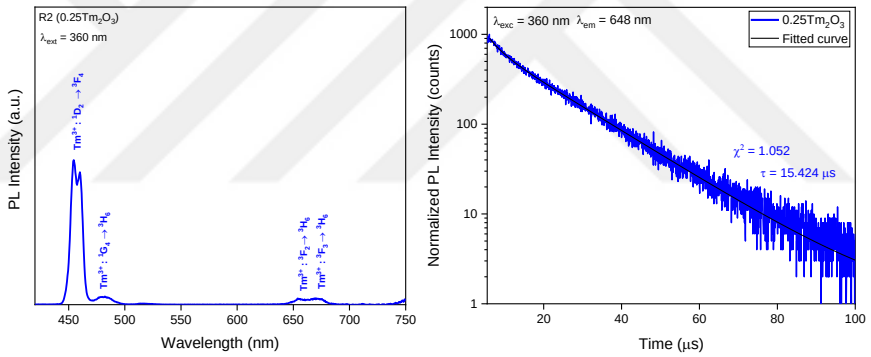


Figure 4.47 a) PL emission spectrum and b) Lifetime analysis for Sample 1

4.2.3.2 PL and Lifetime Analysis of Reference Sample 2 (0.25 Sm_2O_3)

The composition of Reference Sample 2 is as follows: 15% Na_2O, 20% CaO, 5% Al_2O_3, 15% B_2O_3, 45% SiO_2, and 0.25 Sm_2O_3. The Reference Sample 2's PL spectra are shown in Figure 4.48a. Four different peaks associated with Sm^{3+} ions can be seen under 360 nm excitation. When Sm^{3+} ions transition from $^4G_{5/2}$ to ^6H_J (J = 5/2, 7/2, 9/2, and 11/2, respectively), they emit four distinct spectral lines at 565, 602, 648, and 707 nm. The lifetime analysis of Reference Sample 2 is shown in Figure 4.48b, and the values for $\chi 2$ and τ are determined to be 1.043 and 2.09 s, respectively.

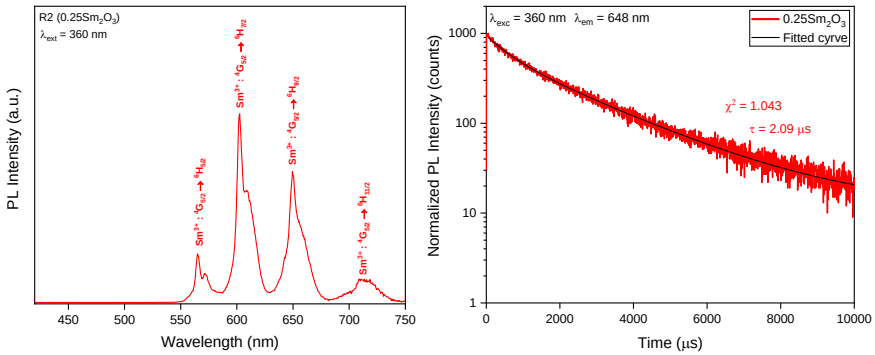


Figure 4.48 a) PL emission spectrum and b) Lifetime analysis for Sample 2

The lifetime values of the best matched red (648 nm) and blue (454 nm) emissions of the Reference Sample 1 and Sample 2, respectively, are 15.10 s and 2.09 s. However, with the chosen $0.25Sm_2O_3 – 0.25Tm_2O_3$ sample, the lifetime values for blue and red emission drop to 12.23 µs and 1.42 µs, respectively. Notably, the selected sample's lanthanide concentration is equal to the total of the lanthanide concentrations in the Reference Sample 1 and Reference Sample 2. This shows a decrease in the lifespan values of all emissions due to an increase in the rate of energy transfer and the quantity of cross-relaxations between lanthanide ions. The significance of the lanthanide concentration in regulating the energy transfer dynamics and lifetime values of emissions in the investigated glass system is highlighted by this conclusion. [92]. Figure 4.49a shows the difference between lifetime graph of Reference Sample 1 and selected sample, and Figure 4.49b shows the difference between lifetime graph of Reference Sample 2 and selected sample.

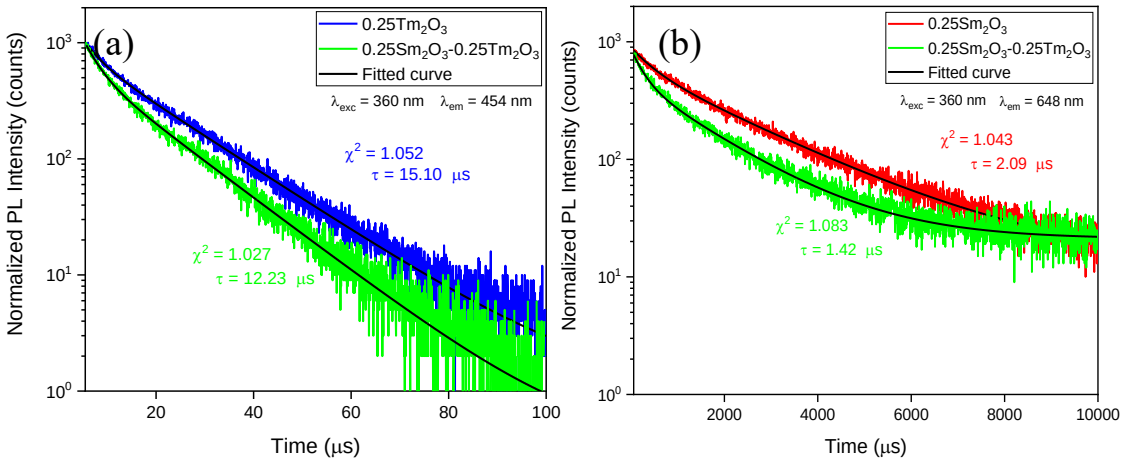


Figure 4.49 Time-resolved PL spectra of (a) $0.25Tm_2O_3$ (Reference Sample 1) and $0.25Sm_2O_3 – 0.25Tm_2O_3$ samples for 454 nm emission, and (b) $0.25Sm_2O_3$ (Reference Sample 2) and $0.25Sm_2O_3 – 0.25Tm_2O_3$ samples for 648 nm emission

Using the Jablonski diagram, the energy transfer process in the chosen $0.25Sm_2O_3$ - $0.25Tm_2O_3$ sample is explained in Figure 4.50. Both Tm^{3+} and Sm^{3+} ions absorb the excitation energy after being excited with 360 nm. Sm^{3+} ions then experience non-radiative energy transfer to the $^4G_{5/2}$ energy state after being stimulated from their $^6H_{5/2}$ ground state to $^4F_{7/2}$, $^4F_{5/2}$, and $^4I1_{3/2}$ excited states. Finally, when they are relaxed to their ^6H_J (J = 5/2, 7/2, 9/2, and 11/2) states, orange and red light are released at 565 nm, 602 nm, 648 nm, and 707 nm wavelengths. Additionally, the emission of blue light at 454 nm is caused by the excitation of Tm^{3+} ions from their $^3H_6$ ground state to the $^1D_2$ excited state, which is followed by relaxation through the $^3F_4$ energy state. Through an Energy Transfer (ET) process, Sm^{3+} ions can simultaneously absorb this relaxed energy, resulting in red emissions. [93]. The previously mentioned lifetime periods are decreased when both Tm^{3+} and Sm^{3+} ions are present in the same structure, as seen in Figure 4.50a and Figure 4.50b, because of the ET transition between Tm^{3+} and Sm^{3+} ions.

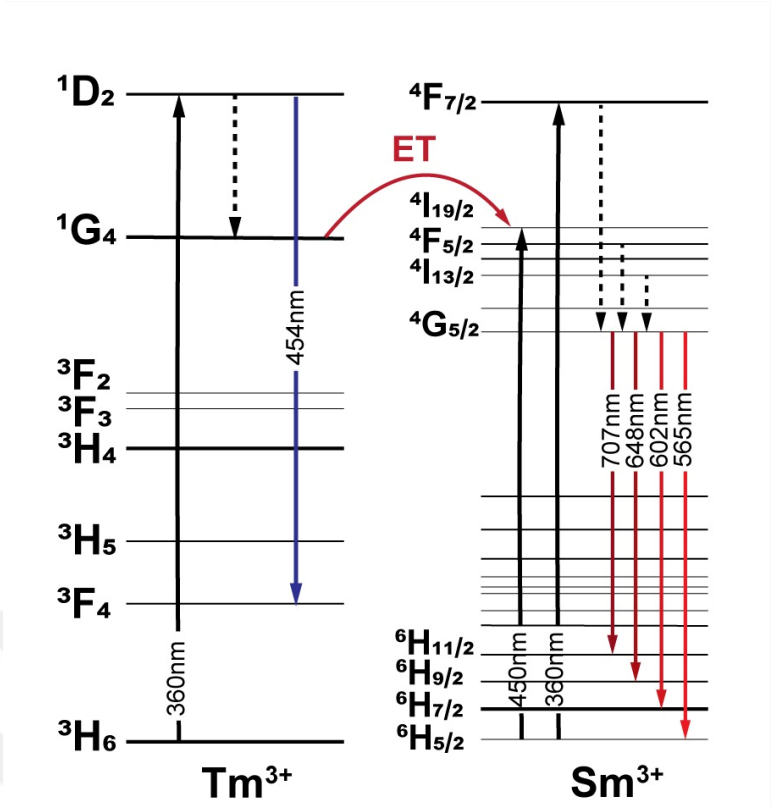


Figure 4.50 Partial Jablonski diagram for selected $0.25Sm_2O_3 – 0.25Tm_2O_3$ sample showing possible energy transfer mechanisms for Sm^{3+} and Tm^{3+} ions under 360 nm excitation

The degree of sample overlap with the absorption spectra of chlorophyll a and b is displayed in Figure 4.52. Chlorophylls a (SRch-a) and b (SRch-b) are discovered to have spectral similarity values of 50% and 39%, respectively, indicating an excellent fit with the spectrum needed for photosynthesis These findings imply that the chosen sample has the ability to offer the required spectral range for chlorophylls, which are essential for driving the photosynthetic process in plants, to efficiently absorb light. It is common knowledge that phytochrome pigment, which controls plant development and growth, functions in the red and far-red regions (600-750 nm), while carotenoids, protein components of chlorophylls, absorb light in the blue region [11,12]. In addition, blue-sensitive cryptochrome and phototropin pigments are involved in a number of plant

responses, including germination, root elongation, and the placement of photosynthetic organelles [94]. As shown in Figure 4.51, the selected $0.25Sm_2O_3$ - $0.25Tm_2O_3$ sample exhibits strong luminescence in the blue and red regions, which match the locations of absorption of the proteins and pigments mentioned previously. As a result, it is expected that a Sm^{3+} and Tm^{3+} co-doped luminescent glass-based LED created using the chosen sample may have a good effect on the phototropic and photomorphogenetic responses of various plant species.

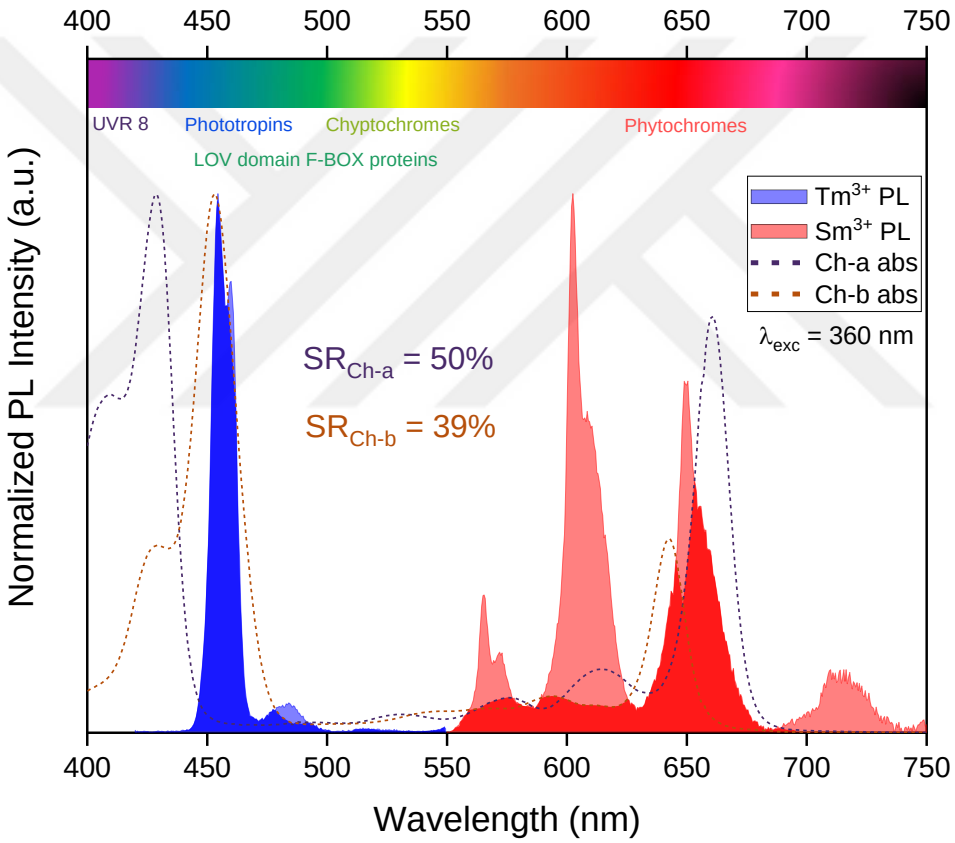


Figure 4.51 Normalized PL spectra of the selected $0.25Sm_2O_3 – 0.25Tm_2O_3$ sample, fitted onto the absorption profiles of Chlorophyll a and b pigments, with $SR_{Ch\text{-}a}$ and $SR_{Ch\text{-}b}$ indicating the degree of spectrum overlap with the respective pigments.

4.2.4 Temperature Dependent PL Analysis

The heat resistance of the glasses is measured using temperature-dependent PL analysis, starting at room temperature and gradually increasing the temperature by 25 °C up to 300 °C. As shown in Figure 4.52a, phonon-assisted relaxations between lanthanide ions cause the PL emission intensities of Sm^{3+} and Tm^{3+} ions to significantly decrease as temperature rises. However, there is no change in the band positions with temperature for Sm^{3+} and Tm^{3+} ions. These findings show that the selected sample can endure the typical operating temperature range of commercial LED chips and that there will be little loss of luminescent characteristics when the sample is used with a commercial UV LED chip. In addition, experiments involving heating-cooling cycles are carried out up to five times, with consecutive cycles ranging from 25 to 300 °C, to determine the impact of temperature on the PL intensity of Sm^{3+} and Tm^{3+} ions. The PL emission intensities are not considerably impacted by heating-cooling cycles, as seen in Figure 4.52b. This observation suggests that the $0.25Sm_2O_3$ - $0.25Tm_2O_3$ sample has good thermal stability as evidenced by the PL properties being stable even after numerous heating-cooling cycles. This result provides additional proof that the chosen sample is appropriate for possible uses in conjunction with commercial UV LED chips, where fluctuations in temperature are anticipated during operation.

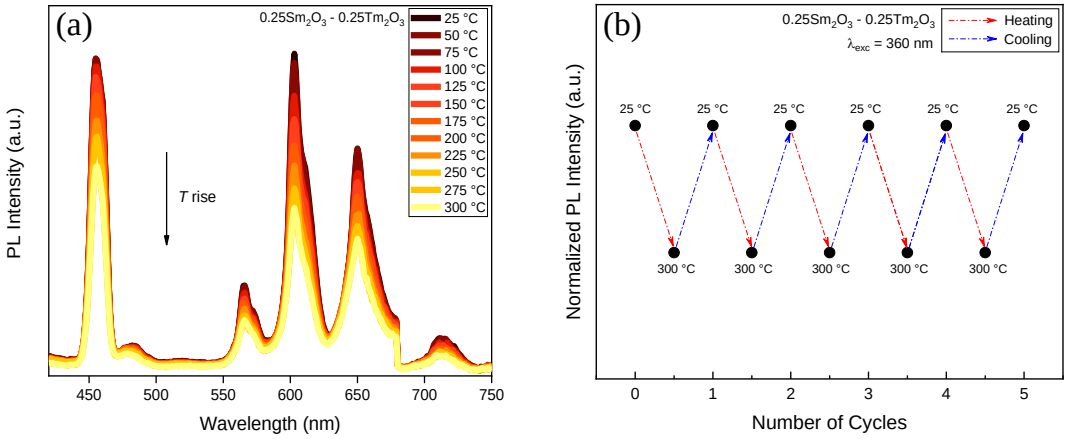


Figure 4.52 a) Temperature-dependent PL emission spectra, b) heating-cooling cycles from 25 °C to 300 °C for the selected $0.25Sm_2O_3 – 0.25Tm_2O_3$ sample (all stability measurements are conducted under 360 nm excitation)

4.2.5 Plant Growth LED Studies

As illustrated in Figure 4.53, a proof-of-concept plant growth LED system (Sm^{3+} and Tm^{3+} co-doped luminescent glass-based plant growth LED) is created by combining the chosen sample of $0.25Sm_2O_3$ - $0.25Tm_2O_3$ to a readily accessible 360 nm UV LED chip. This LED generates light constantly in the red and blue color spectrum, with an intensity of 80% red and 20% blue ($R_{80}B_{20}$), which roughly resembles the absorption spectra of the pigment's chlorophyll a/b, carotenoid, and phytochrome.

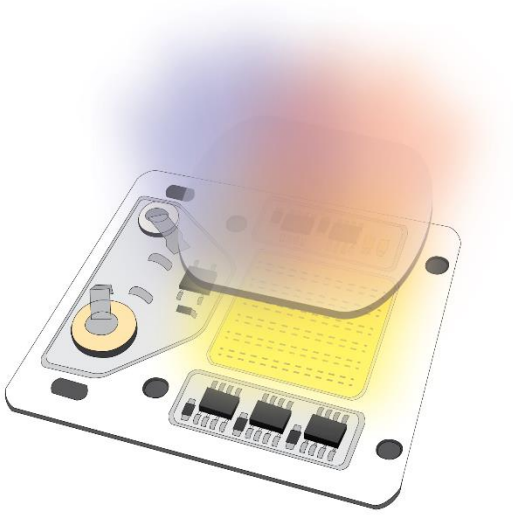


Figure 4.53 Sm^{3+} and Tm^{3+} co-doped luminescent glass-based plant growth LED

Two LED plates with adjustable light intensities are made using commercial white and plant growth LEDs along with Sm^{3+} and Tm^{3+} co-doped luminescent glass-based plant growth LEDs (only in the experimental group), as shown in Figure 4.54, to create an experimental and control group. LED plates employ aluminum substrates, and both contain cooling channels and fans to prevent stability problems that could result from high power consumption and lengthy operating cycles.



Figure 4.54 Experimental LED plate

The light output of both LED panels is precisely controlled to maintain a 150 μmol $m^{-2}s^{-1}$ photosynthetic photon flux density in the 400-700 nm wavelength range. The experimental group is subjected to two Sm^{3+} and Tm^{3+} co-doped luminescent glass-based plant growth LEDs that emit 33 μmol $m^{-2}s^{-1}$ of $R_{80}B_{20}$, along with an 84 μmol $m^{-2}s^{-1}$ commercial white LED, carefully arranged on the LED plate as shown in Figure 4.54. The control group, on the other hand, is made by combining a 66 μmol $m^{-2}s^{-1}$ $R_{60}B_{40}$ (60% red and 40% blue) commercial plant growth LED with an 84 μmol $m^{-2}s^{-1}$ commercial white LED. As can be seen in Figure 4.55, these two separate lighting systems are then put in the plant growth chamber and hung 50 cm above the plant's highest point using a pulley system. On both sides of the plant growth chamber, photoperiods with a daily light integral of 7.8 mol $m^{-2}day^{-1}$ are applied for 14 h launching at 8:00 am and terminating at 22:00 pm.

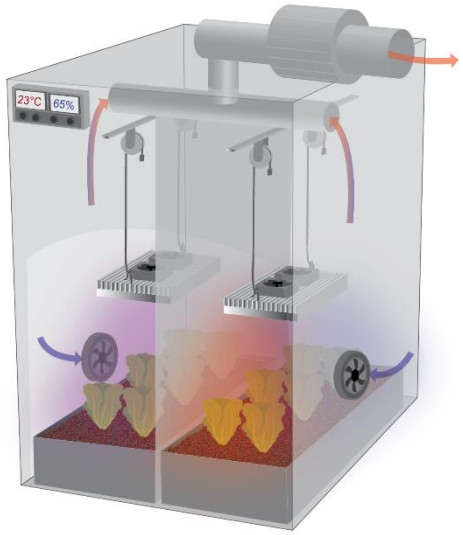


Figure 4.55 Plant growth chamber (the arrows represent how the temperature within the cabinet is controlled by a motorized ventilation and fans through air circulation)

The emission spectra of a chosen $0.25Sm_2O_3 – 0.25Tm_2O_3$ sample and a commercial UV LED chip are displayed in Figure 4.56a. Upon activation of the UV LED chip at a wavelength of 360 nm, distinct emission bands from Sm^{3+} ions at 565, 602, 648, and 707 nm, as well as from Tm^{3+} ions at 454 and 482 nm, are plainly visible.

Once the LEDs are attached to the plates, several tests stimulating a 14-hour photoperiod are conducted on them to evaluate their operational stability. The light output and temperature of the LEDs are measured using an IR thermometer and an Asensetek Lighting Passport Pro Spectrometer. Figure 4.56b shows the average operating temperatures and light intensities of commercial and designed growth LEDs. The outcomes clearly demonstrate that the cooling mechanism is successful in maintaining the LEDs' temperature within accepted limits. Additionally, during the course of the whole 14-hour photoperiod, two competing LED systems successfully maintain a photosynthetic photon flux density (PPFD) at a level of about 66 μmol $m^{-2}s^{-1}$. The fact that there is no discernible change in the light output and operating temperature of the LEDs over time demonstrates that they are not affected by issues like fatigue or performance degradation throughout the photoperiodic cycle.

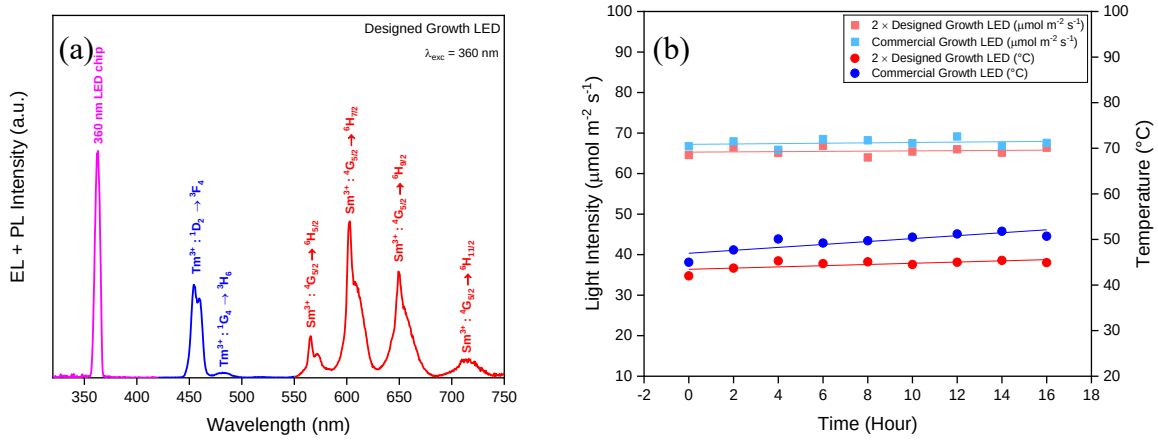


Figure 4.56 a) Emission spectra of commercial UV LED chip and $0.25Sm_2O_3 – 0.25Tm_2O_3$ sample, b) comparison of operation stability of commercial and designed growth LEDs attached on LED plates.

Figure 4.57a shows a visual comparison of lettuce plants from the experimental and control groups at the conclusion of the culture experiment, while Figure 4.57b shows the group of lettuce plants produced under the experimental LED plate at days 28 and 35 of growth. As is evident, the experimental group's lettuce appears to have slightly longer and wider leaves than the control group's lettuce.

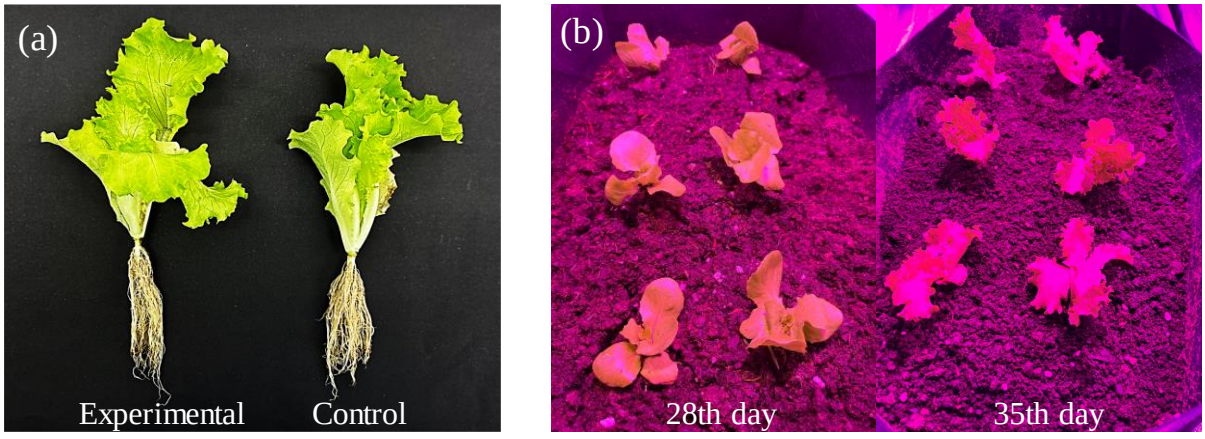


Figure 4.57 a) The grown lettuce under experimental and control LED plates, with experimental lettuce on the left and control lettuce on the right, and. b) group of lettuce grown under the experimental LED plate at 28th and 35th day of cultivation.

According to the findings in Table 4.2 the experimental group has more plant height, fresh and dry weight, and leaf number than the control group, however the experimental group has lower stem diameter and S/R. In addition, the experimental group's carotenoid, chlorophyll-a, and b contents are slightly greater than those of the control group.

Table 4.2 Comparison of morphological characteristics and chlorophyll content between lettuce grown in experimental and control groups.

Plant Parameters	Experimental Group	Control Group
Plant Height (cm)	12.34	11.16
Fresh Weight (FW) (g)	7.47	6.73
Dry Weight (DW) (g)	0.37	0.35
Stem Diameter (mm)	6.20	6.53
Leaf Number	11	10
Ratio of Shoot and Root (S/R)	2.59	2.67
Chlorophyll-a (Chl-a) (mg/g)	0.651	0.537
Chlorophyll-b (Chl-b) (mg/g)	0.028	0.023
Carotenoid (mg/g)	0.201	0.165

The results of the study collectively imply that employing the use of Sm^{3+} and Tm^{3+} co-doped luminescent glass-based plant growth LED can boost plant growth and crop quality. The future of indoor horticulture and plant growing facilities will be significantly impacted by these findings.

4.3 Conclusion and Future Outlook

As a result, glass samples co-doped with Sm_2O_3 and Tm_2O_3 and with different lanthanide molar concentrations were successfully made utilizing the conventional melt-quenching technique. Based on its higher photoluminescence (PL) intensities, 56% quantum yield value, and capacity to preserve emission characteristics at high temperatures under 360 nm illumination, the $0.25Sm_2O_3$ and $0.25Tm_2O_3$ co-doped sample was selected from among the prepared samples. According to the study, this sample's blue and red emissions efficiently contributed to plant development by covering 50% and 39%, respectively, of the chlorophyll a and b absorption spectra. As a result of these findings, an experimental

plant growth LED device was developed through coupling the chosen sample to a 360 nm LED chip, and a control LED device was built using a commercial plant growth LED for comparison. In comparison to the commercial plant growth LED, the experimental plant growth LED device increased plant height, weight, number of leaves, chlorophyll a, b, and carotenoid content, but it lowered root diameter and shoot-to-root ratio. The results of the study supported the argument that the experimental plant growth LED device developed had exceptional optical qualities and was an effective light source for indoor agricultural applications. This study demonstrates that there's potential for creating indoor farming methods that are more productive. To address issues like food crisis and farmland loss, future research may extend this method to further crop species.

1. All synthesized Sm_2O_3-Tm_2O_3 doped glasses have optically high transparency, and all samples have sharp and high PL emission peaks.

2. After 360 nm excitation, Sm_2O_3-Tm_2O_3 doped glass samples show blue and red emissions and have high PLQY values.

3. CIE color coordinates of glass samples shift towards (x: 0.4781, y: 0.2730) to (x: 0.4664, y: 0.2639) with varying amount of lanthanide ion concentration. There was no proportional change in the CRI values of the samples depending on the concentration.

4. Investigations into photoluminescence revealed that the amount (intensity) of light produced by the sample is not directly correlated with the concentration of rare earth ions. owing to cross-relaxation. The intensity of light emitted by the glass samples with high overall rare earth concentration was often lower than the samples with low overall RE concentration during transitions between the identical RE ions.

5. Temperature Dependent PL analysis applied to the selected 0.25 Sm_2O_3-0.25 Tm_2O_3 sample proved that the materials can withstand high temperatures.

6. The PL radiation peaks of the selected 0.25 Sm_2O_3-0.25 Tm_2O_3 sample and the absorbance peaks of chlorophyll a and b overlap. This proves that the LEDs created with these samples can be used in plant growth.

7. As a result of the plant experiments, it has been proven that the experimental group formed with the 0.25 Sm_2O_3-0.25 Tm_2O_3 sample contributes more to plant growth than commercial LEDs.

8. This study proves that plant growth LEDs constructed with 0.25 Sm_2O_3-0.25 Tm_2O_3 for lighting systems, which have a very important place in indoor agricultural applications, are of great importance and can provide solutions to problems such as reduction of agricultural lands and famine that may be encountered in the future.

REFERENCES

[1] R.K. Mall, A. Gupta, G. Sonkar, “Effect of climate change on agricultural crops, current developments in biotechnology and bioengineering: Crop modification, nutrition, and food production”. (2017) 23–46. https://doi.org/10.1016/B978-0-444-63661-4.00002-5.

[2] F. Mestre-Sanchís and M. L. Feijóo-Bello, “Climate change and its marginalizing effect on agriculture,” Ecological Economics, vol. 68, no. 3, pp. 896–904, Jan. 2009, doi: 10.1016/j.ecolecon.2008.07.015.

[3] R. Anderson, P. E. Bayer, and D. Edwards, “Climate change and the need for agricultural adaptation,” *Current Opinion in Plant Biology*, vol. 56, pp. 197–202, Aug. 2020, doi: 10.1016/j.pbi.2019.12.006.

[4] H. Mempel, I. Jüttner, and S. Wittmann, “The potentials of indoor farming for plant production,” at - *Automatisierungstechnik*, vol. 69, no. 4, pp. 287–296, Apr. 2021, doi: 10.1515/auto-2020-0044.

[5] M. Agovino, M. Casaccia, M. Ciommi, M. Ferrara, and K. Marchesano, “Agriculture, climate change and sustainability: The case of EU-28,” *Ecological Indicators*, vol. 105, pp. 525–543, Oct. 2019, doi: 10.1016/j.ecolind.2018.04.064.

[6] M. de Wit, V. C. Galvão, and C. Fankhauser, “Light-Mediated Hormonal Regulation of Plant Growth and Development,” *Annual Review of Plant Biology*, vol. 67, no. 1, pp. 513–537, Apr. 2016, doi: 10.1146/annurev-arplant-043015-112252.

[7] N. Fukuda, “Plant Growth and Physiological Responses to Light Conditions,” *Plant Factory Using Artificial Light*, pp. 71–77, 2019, doi: 10.1016/b978-0-12-813973-8.00008-7.

[8] H. Dou and G. Niu, “Plant responses to light,” *Plant Factory*, pp. 153–166, 2020, doi: 10.1016/b978-0-12-816691-8.00009-1.

[9] M. Taniguchi and J. S. Lindsey, “Absorption and Fluorescence Spectral Database of Chlorophylls and Analogues,” *Photochemistry and Photobiology*, vol. 97, no. 1, pp. 136–165, Nov. 2020, doi: 10.1111/php.13319.

[10] M. C. Snowden, K. R. Cope, and B. Bugbee, “Sensitivity of Seven Diverse Species to Blue and Green Light: Interactions with Photon Flux,” *PLOS ONE*, vol. 11, no. 10, p. e0163121, Oct. 2016, doi: 10.1371/journal.pone.0163121.

[11] T. Shinomura, K. Uchida, and M. Furuya, “Elementary Processes of Photoperception by Phytochrome A for High-Irradiance Response of Hypocotyl Elongation in Arabidopsis,” *Plant Physiology*, vol. 122, no. 1, pp. 147–156, Jan. 2000, doi: 10.1104/pp.122.1.147.

[12] A. Sancar, “Structure and Function of DNA Photolyase and Cryptochrome Blue-Light Photoreceptors,” *Chemical Reviews*, vol. 103, no. 6, pp. 2203–2238, Apr. 2003, doi: 10.1021/cr0204348.

[13] Z. Zhou et al., “Dy^{3+}@Mn^{4+}co-doped $Ca_{14}Ga_{10-m}Al_mZn_6O_{35}$far-red emitting phosphors with high brightness and improved luminescence and energy transfer properties for plant growth LED lights,” *Journal of Materials Chemistry C*, vol. 5, no. 32, pp. 8201–8210, 2017, doi: 10.1039/c7tc01716b.

[14] Z. Zhou, Y. Li, M. Xia, Y. Zhong, N. Zhou, and H. T. (Bert) Hintzen, “Improved luminescence and energy-transfer properties of Ca14Al10Zn6O35:Ti^{4+}, Mn^{4+} deep-red-emitting phosphors with high brightness for light-emitting diode (LED) plant-growth lighting,” *Dalton Transactions*, vol. 47, no. 38, pp. 13713–13721, 2018, doi: 10.1039/c8dt02991a.

[15] X. Yang et al., “Facile synthesis of the desired red phosphor $Li_2Ca_2Mg_2Si_2N_6$:Eu^{2+} for high CRI white LEDs and plant growth LED device,” *Journal of the American Ceramic Society,* vol. 103, no. 3, pp. 1773–1781, Nov. 2019, doi: 10.1111/jace.16858.

[16] M. Xia et al., “Enhanced photoluminescence and energy transfer performance of $Y_3Al_4GaO_{12}$:Mn^{4+}, Dy^{3+} phosphors for plant growth LED lights,” *RSC Advances*, vol. 9, no. 16, pp. 9244–9252, 2019, doi: 10.1039/c9ra00700h.

[17] R. Anderson, P. E. Bayer, and D. Edwards, “Climate change and the need for agricultural adaptation,” *Current Opinion in Plant Biology,* vol. 56, pp. 197–202, Aug. 2020, doi: 10.1016/j.pbi.2019.12.006.

[18] M. Agovino, M. Casaccia, M. Ciommi, M. Ferrara, and K. Marchesano, "Agriculture, climate change and sustainability: The case of EU-28," *Ecological Indicators*, vol. 105, pp. 525–543, Oct. 2019, doi: 10.1016/j.ecolind.2018.04.064.

[19] S. Kotiranta, S. Siipola, T. M. Robson, P. J. Aphalo, and T. Kotilainen, "LED lights can be used to improve the water deficit tolerance of tomato seedlings grown in greenhouses," *Acta Horticulturae*, no. 1107, pp. 107–112, Dec. 2015, doi: 10.17660/actahortic.2015.1107.14.

[20] M. Anpo, H. Fukuda, and T. Wada, "Introduction: Artificial Light-Type Plant Factories—Outline and a Vision for the Future," *Plant Factory Using Artificial Light*, pp. xxiii–xxviii, 2019, doi: 10.1016/b978-0-12-813973-8.10000-4.

[21] Q. Peng and Q. Zhou, "Effects of enhanced UV-B radiation on the distribution of mineral elements in soybean (Glycine max) seedlings," *Chemosphere*, vol. 78, no. 7, pp. 859–863, Feb. 2010, doi: 10.1016/j.chemosphere.2009.11.050.

[22] Eissa Piri, "Effects of UV irradiation on plants," *African Journal of Microbiology Research*, vol. 5, no. 14, Jul. 2011, doi: 10.5897/ajmr11.263.

[23] H. Kim and S. Hwang, "The Growth and Development of 'Mini Chal' Tomato Plug Seedlings Grown under Various Wavelengths Using Light Emitting Diodes," *Agronomy*, vol. 9, no. 3, p. 157, Mar. 2019, doi: 10.3390/agronomy9030157.

[24] B. Bugbee, "Toward an optimal spectral quality for plant growth and development: the importance of radiation capture," *Acta Horticulturae*, no. 1134, pp. 1–12, May 2016, doi: 10.17660/actahortic.2016.1134.1.

[25] A. Sæbø, T. Krekling, and M. Appelgren, "Light quality affects photosynthesis and leaf anatomy of birch plantlets in vitro," *Plant Cell, Tissue and Organ Culture*, vol. 41, no. 2, pp. 177–185, May 1995, doi: 10.1007/bf00051588.

[26] K.-H. Son, J.-H. Park, D. Kim, and M.-M. Oh, "Leaf Shape Index, Growth, and Phytochemicals in Two Leaf Lettuce Cultivars Grown under Monochromatic Light-emitting Diodes," *Korean Journal of Horticultural Science and Technology*, vol. 30, no. 6, pp. 664–672, Dec. 2012, doi: 10.7235/hort.2012.12063.

[27] K.-H. Son and M.-M. Oh, “Growth, Photosynthetic And Antioxidant Parameters of Two Lettuce Cultivars As Affected By Red, Green, And Blue Light-Emitting Diodes,” *Horticulture, Environment, and Biotechnology*, vol. 56, no. 5, pp. 639–653, Oct. 2015, doi: 10.1007/s13580-015-1064-3.

[28] G. Samuolienė, A. Urbonavičiūtė, P. Duchovskis, Z. Bliznikas, P. Vitta, and A. Žukauskas, “Decrease in Nitrate Concentration in Leafy Vegetables Under a Solid-state Illuminator,” *HortScience*, vol. 44, no. 7, pp. 1857–1860, Dec. 2009, doi: 10.21273/hortsci.44.7.1857.

[29] S. D. Carvalho and K. M. Folta, “Environmentally Modified Organisms – Expanding Genetic Potential with Light,” *Critical Reviews in Plant Sciences*, vol. 33, no. 6, pp. 486–508, Jun. 2014, doi: 10.1080/07352689.2014.929929.

[30] Xin, J., Liu, L., Song, S., Chen, R., & Sun, G. (2015). “Growth and Quality of Chinese Kale Grown Under Different LEDs”. *Agric Sci Technol, 16*(1), 68-69.

[31] Z.-H. Bian, R.-F. Cheng, Q.-C. Yang, J. Wang, and C. Lu, “Continuous Light from Red, Blue, and Green Light-emitting Diodes Reduces Nitrate Content and Enhances Phytochemical Concentrations and Antioxidant Capacity in Lettuce,” *Journal of the American Society for Horticultural Science,* vol. 141, no. 2, pp. 186–195, Mar. 2016, doi: 10.21273/jashs.141.2.186.

[32] W. G. Owen and R. G. Lopez, “End-of-production Supplemental Lighting with Red and Blue Light-emitting Diodes (LEDs) Influences Red Pigmentation of Four Lettuce Varieties,” *HortScience*, vol. 50, no. 5, pp. 676–684, May 2015, doi: 10.21273/hortsci.50.5.676.

[33] C. C. S. Nicole et al., “Lettuce growth and quality optimization in a plant factory,” *Acta Horticulturae*, no. 1134, pp. 231–238, May 2016, doi: 10.17660/actahortic.2016.1134.31.

[34] K. Taulavuori, V. Hyöky, J. Oksanen, E. Taulavuori, and R. Julkunen-Tiitto, “Species-specific differences in synthesis of flavonoids and phenolic acids under increasing periods of enhanced blue light,” *Environmental and Experimental Botany*, vol. 121, pp. 145–150, Jan. 2016, doi: 10.1016/j.envexpbot.2015.04.002.

[35] Çağlayan, N., & Ertekin, C. (2018). "Farklı Dalga Boylu LED Işıklarının Yeşil Yapraklı Bitkilerin Gelişimi Üzerindeki Etkileri". *Tarım Makinaları Bilimi Dergisi (Journal of Agricultural Machinery Science), 14*(2), 105-114.

[36] Y. Yan, C. Luo, S. Ling, J. Liang, S. Liao, and Y. Huang, "Enhancing quantum efficiency and thermal stability in $Gd_2SrAl_2O_7$: Mn^{4+}, Bi^{3+}, Na^+ far-red emitting phosphor by energy transfer and cation substitution strategy for indoor plant growth LED lighting," *Journal of Alloys and Compounds*, vol. 947, p. 169609, Jun. 2023, doi: 10.1016/j.jallcom.2023.169609.

[37] L. Vijayalakshmi and J. D. Baek, "Conversion of UV light to dazzling reddish orange light with robust color purity for plant growth in biocompatible glasses," *Journal of Non-Crystalline Solids*, vol. 589, p. 121662, Aug. 2022, doi: 10.1016/j.jnoncrysol.2022.121662.

[38] L. Vijayalakshmi, K. N. Kumar, K. M. Rao, J. D. Baek, and P. Hwang, "Biocompatible lithium zinc borate glasses activated with Sm^{3+}/Eu^{3+} for glass greenhouse," *Ceramics International*, vol. 48, no. 12, pp. 17969–17974, Jun. 2022, doi: 10.1016/j.ceramint.2021.12.263.

[39] C. Ming, F. Song, L. An, and X. Ren, "Research phosphate glass on turning sunlight into red light for glass greenhouse," *Materials Letters*, vol. 137, pp. 117–119, Dec. 2014, doi: 10.1016/j.matlet.2014.08.149.

[40] T.-S. Lv, X.-H. Xu, D.-C. Zhou, H.-L. Yu, and J.-B. Qiu, "Efficient multi-wavelength-driven spectral conversion from ultraviolet to visible in transparent borosilicate glasses," *Ceramics International*, vol. 40, no. 8, pp. 12367–12373, Sep. 2014, doi: 10.1016/j.ceramint.2014.04.085.

[41] C. Ming, F. Song, L. An, and X. Ren, "Turning ultraviolet-green into red light in transparent phosphate glasses for greenhouses," *Applied Physics Letters*, vol. 102, no. 14, p. 141903, Apr. 2013, doi: 10.1063/1.4801465.

[42] C. Ming, F. Song, X. Ren, and L. An, "Highly efficient reddish orange emission in Mn^{2+}/Eu^{3+} co-doped phosphate glasses for greenhouse," *Applied Physics Letters*, vol. 103, no. 4, p. 041906, Jul. 2013, doi: 10.1063/1.4816597.

[43] Z. Zhang et al., "Novel red-emitting CsPb1−Ti I_3 perovskite QDs@glasses with ambient stability for high efficiency white LEDs and plant growth LEDs,"

Chemical Engineering Journal, vol. 378, p. 122125, Dec. 2019, doi: 10.1016/j.cej.2019.122125.

[44] Z. Zhang et al., "Coexisting $CsPbCl_3$:$CsPbI_3$ perovskite nanocrystal glasses with high luminescence and stability," *Chemical Engineering Journal*, vol. 385, p. 123415, Apr. 2020, doi: 10.1016/j.cej.2019.123415.

[45] Y. Chen, L. Shen, J. Liu, X. Liang, and W. Xiang, "Eco-friendly Mn-doped $CsPbCl_3$ perovskite nanocrystal glass with blue-red emission for indoor plant lighting," *Journal of the American Ceramic Society*, vol. 104, no. 6, pp. 2579–2587, Feb. 2021, doi: 10.1111/jace.17644.

[46] J. Liu et al., "Highly luminescent and ultra-stable cesium lead halide perovskite nanocrystal glass for plant-growth lighting engineering," *Journal of Materials Chemistry C*, vol. 7, no. 43, pp. 13606–13612, 2019, doi: 10.1039/c9tc04799a.

[47] Y. Liang et al., "Towards control facilities for mimicking plant growth optimum action spectrum: Efficient near-ultraviolet to far-red light-conversion in Cr^{3+}-doped rare-earth aluminate phosphors," *Chemical Engineering Journal*, vol. 454, p. 140235, Feb. 2023, doi: 10.1016/j.cej.2022.140235.

[48] Y. Zhang et al., "Improving moisture stability of $SrLiAl_3N_4$:Eu^{2+} through phosphor-in-glass approach to realize its application in plant growing LED device," *Journal of Colloid and Interface Science*, vol. 545, pp. 195–199, Jun. 2019, doi: 10.1016/j.jcis.2019.03.032.

[49] M. Li et al., "Cr^{3+} doped $ZnGa_2O_4$ far-red emission phosphor-in-glass: Toward high-power and color-stable plant growth LEDs with responds to all of phytochrome," *Materials Research Bulletin*, vol. 108, pp. 226–233, Dec. 2018, doi: 10.1016/j.materresbull.2018.09.014.

[50] M. Li et al., "F enhanced luminescence performance of $SrLu_2O_4$:Ce^{3+} glass ceramic for superior high-power artificial horticultural LEDs," *Ceramics International*, vol. 46, no. 13, pp. 21560–21568, Sep. 2020, doi: 10.1016/j.ceramint.2020.05.259.

[51] P. N. Parale, A. R. Kadam, K. V. Dabre, and S. J. Dhoble, "Spectroscopic investigation of $KBa_2(PO_3)_5$: Mn^{4+} activated glasses for plant cultivation

applications," *Materials Letters*: X, vol. 18, p. 100191, Jun. 2023, doi: 10.1016/j.mlblux.2023.100191.

[52] L. Xu et al., "Cu^{2+} and Cr^{3+} doped borate glasses and glass-ceramics as light conversion materials for plant photosynthesis," *Optical Materials*, vol. 137, p. 113614, Mar. 2023, doi: 10.1016/j.optmat.2023.113614.

[53] W. Wang, Z. Huang, H. Gao, X. Cheng, and Y. Mao, "Broadband emission from $Ce^{3+}/Mn^{2+}/Yb^{3+}$ tri-doped oxyfluoride glasses for glass greenhouse," *Optical Materials*, vol. 62, pp. 494–498, Dec. 2016, doi: 10.1016/j.optmat.2016.10.037.

[54] C. Zhu, X. Zhang, and H. Ma, "Sb/Mn co-doped oxyfluoride silicate glasses for potential applications in photosynthesis," *Journal of Luminescence*, vol. 171, pp. 198–201, Mar. 2016, doi: 10.1016/j.jlumin.2015.11.004.

[55] D. Hebert et al., "Luminescent quantum dot films improve light use efficiency and crop quality in greenhouse horticulture," *Frontiers in Chemistry*, vol. 10, Oct. 2022, doi: 10.3389/fchem.2022.988227.

[56] D. V. Yanykin, D. E. Burmistrov, A. V. Simakin, J. A. Ermakova, and S. V. Gudkov, "Effect of Up-Converting Luminescent Nanoparticles with Increased Quantum Yield Incorporated into the Fluoropolymer Matrix on Solanum lycopersicum Growth," *Agronomy*, vol. 12, no. 1, p. 108, Jan. 2022, doi: 10.3390/agronomy12010108.

[57] A. V. Simakin, V. V. Ivanyuk, A. S. Dorokhov, and S. V. Gudkov, "Photoconversion Fluoropolymer Films for the Cultivation of Agricultural Plants Under Conditions of Insufficient Insolation," *Applied Sciences*, vol. 10, no. 22, p. 8025, Nov. 2020, doi: 10.3390/app10228025.

[58] C. Zhu, X. Liang, Y. Yang, and G. Chen, "Luminescence properties of Tb doped and Tm/Tb/Sm co-doped glasses for LED applications," *Journal of Luminescence*, vol. 130, no. 1, pp. 74–77, Jan. 2010, doi: 10.1016/j.jlumin.2009.07.023.

[59] Runkle, E. (2021, August). "Increasing the Daily Light Integral". *Greenhouse Product News*, 50.

[60] J. Pereira, A. M. Mouazen, M. Foo, and H. Ahmed, "A framework of artificial light management for optimal plant development for smart greenhouse

application," *PLOS ONE*, vol. 16, no. 12, p. e0261281, Dec. 2021, doi: 10.1371/journal.pone.0261281.

[61] H. A. Ahemd, A. A. Al-Faraj, and A. M. Abdel-Ghany, "Shading greenhouses to improve the microclimate, energy and water saving in hot regions: A review," *Scientia Horticulturae*, vol. 201, pp. 36–45, Mar. 2016, doi: 10.1016/j.scienta.2016.01.030.

[62] M.-T. Krieger, J. Ditton, H. Albrecht, L. Linderl, J. Kollmann, and L. H. Teixeira, "Effects of shading and site conditions on vegetative and generative growth of a native grassland invader," *Ecological Engineering*, vol. 178, p. 106592, May 2022, doi: 10.1016/j.ecoleng.2022.106592.

[63] M. W. van Iersel, "Optimizing LED Lighting in Controlled Environment Agriculture," *Light Emitting Diodes for Agriculture*, pp. 59–80, 2017, doi: 10.1007/978-981-10-5807-3_4.

[64] J. Lin et al., "Perovskite Quantum Dots Glasses Based Backlit Displays," *ACS Energy Letters*, vol. 6, no. 2, pp. 519–528, Jan. 2021, doi: 10.1021/acsenergylett.0c02561.

[65] D. Chen et al., "$CsPbX_3$ (X = Br, I) perovskite quantum dot embedded low-melting phosphosilicate glasses: controllable crystallization, thermal stability and tunable emissions," *Journal of Materials Chemistry C*, vol. 6, no. 25, pp. 6832–6839, 2018, doi: 10.1039/c8tc02407c.

[66] O. Kıbrıslı, E. Erol, A. E. Ersundu, and M. Çelikbilek Ersundu, "CdSe and $CsPbBr_3$ quantum dot Co-doped monolithic glasses as tunable wavelength convertors," *Journal of Physics D*: Applied Physics, vol. 55, no. 10, p. 105301, Nov. 2021, doi: 10.1088/1361-6463/ac3b10.

[67] D. R. Vij, Ed., *Luminescence of Solids*. 1998. doi: 10.1007/b11525310.1007/978-1-4615-5361-8.

[68] B. Valeur and M. N. Berberan-Santos, "A Brief History of Fluorescence and Phosphorescence before the Emergence of Quantum Theory," *Journal of Chemical Education*, vol. 88, no. 6, pp. 731–738, Mar. 2011, doi: 10.1021/ed100182h.

[69] F. Wang and X. Liu, "1.18 - Rare-Earth Doped Upconversion Nanophosphors," *Comprehensive Nanoscience and Technology, D. L. Andrews, G. D. Scholes, and G. P. Wiederrecht, Eds. Amsterdam: Academic Press*, 2011, pp. 607-635.

[70] P. A. M. Dirac, *The Principles of Quantum Mechanics*. 2013. doi: 10.1604/9780198520115.

[71] N. T. Kalyani, H. C. Swart, and S. J. Dhoble, Principles and Applications of Organic Light Emitting Diodes (OLEDs). *Woodhead Publishing Limited*, 2017.

[72] S. D. Carvalho and K. M. Folta, "Environmentally Modified Organisms – Expanding Genetic Potential with Light," *Critical Reviews in Plant Sciences*, vol. 33, no. 6, pp. 486–508, Jun. 2014, doi: 10.1080/07352689.2014.929929.

[73] A. Sæbø, T. Krekling, and M. Appelgren, "Light quality affects photosynthesis and leaf anatomy of birch plantlets in vitro," *Plant Cell, Tissue and Organ Culture*, vol. 41, no. 2, pp. 177–185, May 1995, doi: 10.1007/bf00051588.

[74] E. Erol, N. Vahedigharehchopogh, O. Kıbrıslı, M. Ç. Ersundu, and A. E. Ersundu, "Recent progress in lanthanide-doped luminescent glasses for solid-state lighting applications—a review," *Journal of Physics: Condensed Matter*, vol. 33, no. 48, p. 483001, Sep. 2021, doi: 10.1088/1361-648x/ac22d9.

[75] A. Ivaturi and H. Upadhyaya, "Upconversion and Downconversion Processes for Photovoltaics," in A Comprehensive Guide to Solar Energy Systems: With Special Focus on Photovoltaic Systems, *Elsevier*, 2018, pp. 279–298. doi: 10.1016/B978-0-12-811479-7.00013-0.

[76] W. W. Piper, J. A. DeLuca, and F. S. Ham, "Cascade fluorescent decay in Pr^{3+}-doped fluorides: Achievement of a quantum yield greater than unity for emission of visible light," *Journal of Luminescence*, vol. 8, no. 4, pp. 344–348, Feb. 1974, doi: 10.1016/0022-2313(74)90007-6.

[77] Nakamura, S., and Fasol, G., "The blue laser diode: GaN based light emitters and lasers". *Springer Science and Business Media*, 2013.

[78] R. Zhang, H. Lin, Y. Yu, D. Chen, J. Xu, and Y. Wang, "A new-generation color converter for high-power white LED: transparent Ce^{3+}: YAG phosphor-in-glass," *Laser & Photonics Reviews*, vol. 8, no. 1, pp. 158–164, Dec. 2013, doi: 10.1002/lpor.201300140.

[79] E. Erol, O. Kıbrıslı, M. Çelikbilek Ersundu, and A. E. Ersundu, "Size-controlled emission of long-time durable $CsPbBr_3$ perovskite quantum dots embedded tellurite glass nanocomposites," *Chemical Engineering Journal*, vol. 401, p. 126053, Dec. 2020, doi: 10.1016/j.cej.2020.126053.

[80] G. C. Righini, M. Ferrari, "Photoluminescence of rare-earth--doped glasses," *LA RIVISTA DEL NUOVO CIMENTO*, no. 12, Dec. 2005, doi: 10.1393/ncr/i2006-10010-8.

[81] O. Kıbrıslı, "Lanthanide and/or Quantum Dot Doped Luminescent Glasses/Glass Nanocomposites as Wavelength Convertors for Advanced Opto Electronic Applications [Extractive Metallurgy]", *Yıldız Technical University, Institute of Science.*

[82] M. C. Subin, J. S. Lourence, R. Karthikeyan, and C. Periasamy, "Analysis of materials used for Greenhouse roof covering - structure using CFD," *IOP Conference Series: Materials Science and Engineering*, vol. 346, p. 012068, Apr. 2018, doi: 10.1088/1757-899x/346/1/012068.

[83] B. Bugbee, "Toward an optimal spectral quality for plant growth and development: the importance of radiation capture," *Acta Horticulturae*, no. 1134, pp. 1–12, May 2016, doi: 10.17660/actahortic.2016.1134.1.

[84] E. Erol, O. Kıbrıslı, M. Çelikbilek Ersundu, and A. E. Ersundu, "Color tunable emission from Eu^{3+} and Tm^{3+} co-doped CsPbBr3 quantum dot glass nanocomposites," *Physical Chemistry Chemical Physics*, vol. 24, no. 3, pp. 1486–1495, 2022, doi: 10.1039/d1cp05016h.

[85] B. Valeur and M. N. Berberan-Santos, "A Brief History of Fluorescence and Phosphorescence before the Emergence of Quantum Theory," *Journal of Chemical Education*, vol. 88, no. 6, pp. 731–738, Mar. 2011, doi: 10.1021/ed100182h.

[86] H. K. LICHTENTHALER and A. R. WELLBURN, "Determinations of total carotenoids and chlorophylls a and b of leaf extracts in different solvents," *Biochemical Society Transactions*, vol. 11, no. 5, pp. 591–592, Oct. 1983, doi: 10.1042/bst0110591.

[87] S. Fang, T. Lang, T. Han, M. Cai, S. Cao, L. Peng, B. Liu, Y. Zhong, A.N. Yakovlev, V.I. Korepanov, A novel efficient single-phase dual-emission phosphor with high resemblance to the photosynthetic spectrum of chlorophyll a and b, *Journal of Materials Chemistry C*, vol. 8, 6245–6253, 2020, https://doi.org/10.1039/D0TC00811G.

[88] P. R. Rani et al., "Structural, absorption and photoluminescence studies of Sm^{3+} ions doped barium lead alumino fluoro borate glasses for optoelectronic device applications," *Materials Research Bulletin*, vol. 110, pp. 159–168, Feb. 2019, doi: 10.1016/j.materresbull.2018.10.033.

[89] R. Praveena, K. H. Jang, C. K. Jayasankar, and H. J. Seo, "Optical absorption and fluorescence properties of Tm^{3+}-doped K–Mg–Al phosphate glasses for laser applications," *Journal of Alloys and Compounds*, vol. 496, no. 1–2, pp. 335–340, Apr. 2010, doi: 10.1016/j.jallcom.2010.02.007.

[90] D. Wang et al., "Study on luminescence properties of Tm^{3+}/Tb^{3+}/Eu^{3+} doped germanosilicate glass," *Journal of Non-Crystalline Solids*, vol. 584, p. 121504, May 2022, doi: 10.1016/j.jnoncrysol.2022.121504.

[91] Z. Wu, H. Wu, L. Tang, Y. Li, D. Xiaochun, and Y. Guo, "Fluorescence and energy transfer between Eu^{3+} and Sm^{3+} in single doped and co-doped borate glass," *Journal of Non-Crystalline Solids*, vol. 463, pp. 169–174, May 2017, doi: 10.1016/j.jnoncrysol.2017.03.010.

[92] N. Vahedigharehchopogh, O. Kıbrıslı, A. E. Ersundu, and M. Çelikbilek Ersundu, "Color tunability and white light generation through up-conversion energy transfer in Yb^{3+} sensitized Ho^{3+}/Tm^{3+} doped tellurite glasses," *Journal of Non-Crystalline Solids*, vol. 525, p. 119679, Dec. 2019, doi: 10.1016/j.jnoncrysol.2019.119679.

[93] R. T. Alves, C. M. Trindade, A. C. A. Silva, N. O. Dantas, and A. S. Gouveia-Neto, "White light generation and energy transfer in Tm^{3+}/Tb^{3+}/Sm^{3+} -doped $60TeO_2$. 40ZnO glasses," *Journal of Luminescence*, vol. 227, p. 117543, Nov. 2020, doi: 10.1016/j.jlumin.2020.117543.

[94] E. P. SPALDING and K. M. FOLTA, "Illuminating topics in plant photobiology," *Plant, Cell and Environment*, vol. 28, no. 1, pp. 39–53, Jan. 2005, doi: 10.1111/j.1365-3040.2004.01282. x.

PUBLICATIONS FROM THE THESIS

Papers

1. U. Ekim, E. İlter, E. Özan, Y. Temurhan, M. Çelikbilek Ersundu, and A. E. Ersundu, "Sm^{3+} and Tm^{3+} Co-Doped Luminescent Glasses: Enhancing Indoor Horticulture with Novel Glass-Based Plant Growth LED System," *Physical Chemistry Chemical Physics*, Aug. 2023, doi: 10.1039/D3CP03440B.

Projects

1. YTU Scientific Research Project (BAP) No: FYL-2022-5156 "Development of Glass-Based Color Converters," Researcher, (2022-2023).

International Conferences

1. U. Ekim, A. E. Ersundu, E. İlter, E. Özan, Y. Temurhan, and M. Çelikbilek Ersundu, "Efficient Lighting for Indoor Agriculture: Enhancing Plant Growth with Luminescent Glass-Based LEDs," *11th International Congress on Engineering, Architecture and Design*, July 10-12, 2023, Türkiye.